



HAL
open science

Employing Williams' series for the identification of fracture mechanics parameters from phase-field simulations

Leon M. Kolditz, Samy Dray, Viktor Kosin, Amélie Fau, François Hild, Thomas Wick

► **To cite this version:**

Leon M. Kolditz, Samy Dray, Viktor Kosin, Amélie Fau, François Hild, et al.. Employing Williams' series for the identification of fracture mechanics parameters from phase-field simulations. *Engineering Fracture Mechanics*, 2024. hal-04642699

HAL Id: hal-04642699

<https://hal.science/hal-04642699>

Submitted on 10 Jul 2024

HAL is a multi-disciplinary open access archive for the deposit and dissemination of scientific research documents, whether they are published or not. The documents may come from teaching and research institutions in France or abroad, or from public or private research centers.

L'archive ouverte pluridisciplinaire **HAL**, est destinée au dépôt et à la diffusion de documents scientifiques de niveau recherche, publiés ou non, émanant des établissements d'enseignement et de recherche français ou étrangers, des laboratoires publics ou privés.

Employing Williams' series for the identification of fracture mechanics parameters from phase-field simulations

Leon M. Kolditz¹, Samy Dray^{1,2}, Viktor Kosin^{1,2}, Amélie Fau², François Hild², and Thomas Wick^{1,2}

¹Leibniz Universität Hannover, Institut für Angewandte Mathematik, AG Wissenschaftliches Rechnen, Welfengarten 1, 30167 Hannover, Germany

²Université Paris-Saclay, CentraleSupélec, ENS Paris-Saclay, CNRS, LMPS - Laboratoire de Mécanique Paris-Saclay, 91190 Gif-sur-Yvette, France

July 9, 2024

Highlights

- design of an algorithm to post-process phase-field fracture simulations with Williams' series
- accurate identification of fracture mechanics quantities of interest
- using Williams' series the crack tip position is determined (and not associated with a unique phase-field value)
- numerous convergence results including variations in both numerical and model parameters

Abstract

Fracture mechanics and damage mechanics are two theories that describe the degradation of the bearing capacity of structures. Fracture mechanics is based on a discontinuous description of cracking, while damage mechanics proposes a continuous description of material degradation. These two approaches are often opposed in the literature, from both theoretical and numerical points of view. This work suggests correlating the two approaches by applying Williams' series, usually dedicated to experimental results, to phase-field computations. Williams' series are employed to extract equivalent fracture mechanics parameters as a post-processing step. The proposed analysis based on a fracture mechanics description excludes the fracture process zone. Typical fracture mechanics parameters such as energy release rate, stress intensity factors, fracture process zone size, and crack tip position are determined from the phase-field computations. The approach is illustrated on a two-dimensional structure representing a beam whose notch opening displacement is controlled. The dependence on the choice of the internal length of the phase-field model is studied. Similarities and differences between both modeling routes are discussed.

Keywords: Phase-field fracture; Williams' series; crack tip; stress intensity factor; fracture process zone

1 Introduction

Crack propagation in cementitious materials is a major domain in civil engineering studies to model in-service changes of strength and sealing in structures. Fracture mechanics models have been developed to describe precisely the state of cracks and their propagation within structures. The method was first introduced for brittle materials [23]. Several extensions have been proposed from the lattice method [31], cohesive zone models [8, 30], boundary element methods [16, 43], extended/generalized finite elements [47, 21], or peridynamics [55].

In the case of quasi-brittle materials such as concrete, the crack is generated by a fracture process zone (FPZ), namely, a region with numerous microcracks. Various damage mechanics models can be used to predict the nonlinear behavior inside the FPZ. Several experimental works [62, 32, 15] determined the FPZ size for cementitious materials, which are at the scale of centimeters for decimetric to metric samples. In the case of damage mechanics for concrete, Mazars' model [44] is one of the most commonly used. A regularized extension [18] has been applied using an energetic formulation of crack propagation [30]. Another approach closely related to damage mechanics is the (regularized) phase-field method [39, 46], which is based on a variational approach to fracture [13, 11], considering brittle fracture as an energy minimization problem [19]. A regularization method [2, 3], which was first developed for image segmentation, is utilized to approximate lower-dimensional surfaces with elliptic terms. In such phase-field (variational) fracture approaches, a *phase-field variable* describes the damage state of the material [13, 1, 60, 12, 63, 17, 11, 39, 46, 9].

Due to the smeared transition zone from fully damaged to undamaged states, the crack tip location is usually not precisely defined when using the phase-field method. This point is also mentioned in a recent comparative review [17], the position of the crack tip is not encoded and is approximated. Further fracture mechanics parameters are strain energy release rates, stress intensity factors, fracture process zones, crack tip positions, crack opening displacements, crack densities, crack energies, and bulk energies. Advancements in phase-field fracture have been made for instance using Taylor's expansion of the displacement field for obtaining better crack opening displacements [50], extended finite elements (XFEM) [22] (see also Ref. [52] for XFEM-damage coupling), further studies on level-set and line integral formulas for crack opening displacements [64], or by mesh reconstruction techniques [58] to better locate the crack path and the interface between the fractured and the unbroken zones. However, further quantities of interest (except crack opening displacements) were not computed therein. Crack initiation was investigated in Refs. [40, 56] and specifically in Ref. [56] utilizing a pacman geometry to study stress fields in the vicinity of the crack tip and to identify stress intensity factors.

The phase-field displacement fields can be post-processed with Williams' series. In particular, Williams' series may be employed to compute the previously mentioned fracture mechanics parameters. Williams' series are closed-form solutions to fracture mechanics problems that decompose the resulting displacement and stress fields into unitary fields at several (usually positive) orders [61]. In experimental applications, truncated Williams' series were successfully employed using digital image correlation results [45], for integrated digital image correlation [53, 57], or post-processing finite element solutions in the small scale yielding regime [29]. Correspondence between the phase-field

approach and a coupled (i.e., stress and energy) criterion was investigated in Ref. [48]. In particular, the mechanical significance of the internal length of phase-field models was discussed.

The current work uses a similar pacman geometry as in Refs. [57, 56] but is focused on crack propagation instead of initiation [56]. The key advancement is to employ Williams' series to obtain estimates of crack tip positions, stress intensity factors, and fracture process zone sizes from displacement fields computed by the phase-field method. To carry out computational convergence studies, fine meshes in the phase-field simulations are needed, which yield a high computational cost with more than one million degrees of freedom. To this end, efficient numerical solvers are required. Here, a combined active set Newton-GMRES method [36] was employed in which the linear equation systems are solved with a parallel matrix-free geometric multigrid method [37]. A final fundamental quantity is the energy release rate, for which the J -integral is a well-known extraction method [51], which has also been applied to phase-field simulations [7]. It is proposed to post-process phase-field displacement fields through Williams' series to extract equivalent fracture mechanics parameters. Such an approach is illustrated on a beam represented as a two-dimensional structure whose notch opening displacement is controlled as in actual experiments. The robustness of the approach is shown for various levels of local mesh pre-refinement. The effect of the choice of the internal length on the results of Williams' series during crack propagation is also studied.

The outline of the paper is as follows. In Section 2, the phase-field method is described. Next, Williams' series are introduced in Section 3. Section 4 is devoted to the algorithm. Details are given on how phase-field displacement fields and Williams' series are correlated. In Section 5, numerical investigations are conducted on a notched beam. Several fracture mechanics quantities are extracted. It is shown in Section 6 that various numerical features, such as the mesh discretization or the phase-field regularization parameter, influence the identification set (crack length, energy release rate, stress intensity factors and fracture process zone sizes). The results are discussed in Section 7.

2 Phase-field fracture modeling, discretization, and solution

Let us consider a material in domain $\Omega \subset \mathbb{R}^2$ composed of two subdomains as depicted in Figure 1(a), namely, the bulk B and the fracture surface \mathcal{C} such that $\Omega = B \cup \mathcal{C}$ with $\mathcal{C} = \mathcal{C}_0 \cup \{\underline{x}(s), 0 \leq s \leq l\}$.

Total domain: $\Omega = B \cup \mathcal{C}$

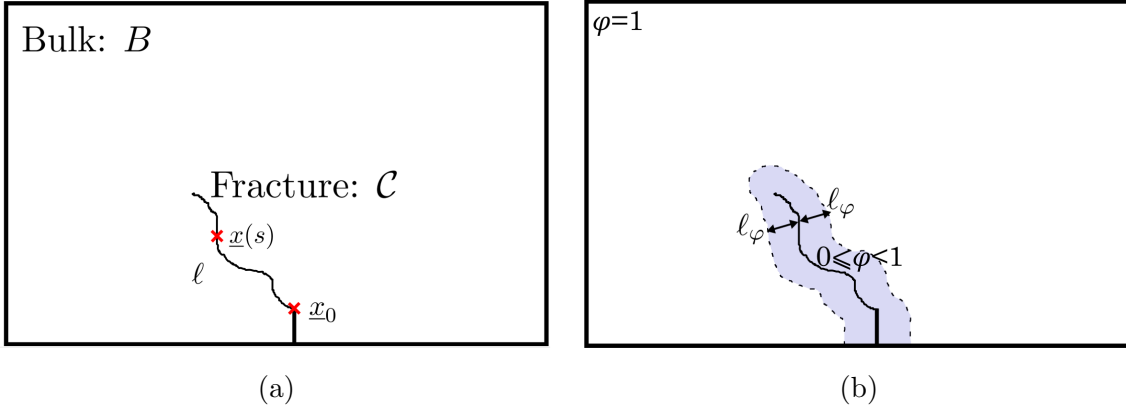


Figure 1: Schematic view of the subdomains of the material with (a) a non-regularized fracture domain and (b) a regularized fracture domain

2.1 Phase-field fracture model

The considered phase-field model [39, 46] is based on a variational formulation [11]. The two following energy contributions [60] are applied

$$\begin{cases} \text{Surface Energy: } \mathcal{E}_s = \int_{\mathcal{C}} \mathcal{G}_c ds \\ \text{Bulk Energy: } \mathcal{E}_b \approx \frac{1}{2} \int_B \underline{\underline{\sigma}} : \underline{\underline{\varepsilon}} dx dy \end{cases} \quad (1)$$

where the parameter $\mathcal{G}_c > 0$ is the critical energy release rate with reference to the Griffith theory [23]. In the present work, this parameter will be assumed to be a material property (i.e., constant). It will not be adjusted with respect to the mesh size or internal length as often performed [13, 56, 64]. Next, $\underline{\underline{\sigma}} \in \mathbb{R}^{D \times D}$ denotes the Cauchy stress tensor, and $\underline{\underline{\varepsilon}} \in \mathbb{R}^{D \times D}$ the infinitesimal strain tensor with $D = 2$ the space dimension. Linear and isotropic elasticity is assumed for the undamaged zones with Young's modulus $E > 0$ and Poisson's ratio $\nu \in [-1, 0.5)$ (i.e., incompressibility is not accounted for in this work). The crack propagates when the energy release rate \mathcal{G} is greater or equal to its critical value \mathcal{G}_c . The displacement field \underline{U}^{PFM} over a time interval $(0, T)$ is calculated using an energetic formulation

$$\underline{U}^{PFM} = \arg \left(\min_{\underline{U} \in V_{\underline{U}}^D(\Omega)} (\mathcal{E}_s(\mathcal{C}) + \mathcal{E}_b(\mathcal{C}, \underline{U})) \right) \quad \text{in } \Omega \times (0, T), \quad (2)$$

with

$$V_{\underline{U}}^D(\Omega) = \{\underline{U} \in V_{\underline{U}} \mid \underline{U} = \underline{U}_D \text{ on } \partial\Omega_D\},$$

the trial space for the displacement field, where $\partial\Omega_D$ is the boundary where the condition $\underline{U} = \underline{U}_D$ is prescribed. The integrals inside \mathcal{E}_s and \mathcal{E}_b must be applied to the same domain to solve Equation (2). The cracked region is regularized from the initial support (Figure 1(a)) to a domain with no discontinuities (Figure 1(b)) using the variable φ and the characteristic (or internal) length ℓ_φ . An Ambrosio-Tortorelli regularization [2, 3] is applied (i.e., the so-called AT-1 functional), where the regularized surface energy reads

$$\mathcal{E}_S^* = \frac{3}{8} \int_{\Omega} \mathcal{G}_c \left(\frac{(1-\varphi)}{\ell_\varphi} + \ell_\varphi \|\nabla\varphi\|^2 \right) dx dy \quad \text{in } \Omega \times (0, T), \quad (3)$$

and the regularized bulk energy

$$\mathcal{E}_b^* = \frac{1}{2} \int_{\Omega} ((1 - \xi)\varphi^2 + \xi)\underline{\underline{\sigma}} : \underline{\underline{\varepsilon}} \, dx dy \quad \text{in } \Omega \times (0, T), \quad (4)$$

with $\ell_{\varphi} > 0$ the phase-field internal length, and $0 < \xi \ll 1$ the bulk regularization parameter. The phase-field variable $0 \leq \varphi(\underline{x}, t) \leq 1$ equals 0 for the cracked region and 1 in the undamaged zone. Finally, the irreversibility condition

$$\partial_t \varphi \leq 0 \quad \text{in } \Omega \times (0, T) \quad (5)$$

is introduced on φ such that healing is excluded.

2.2 Discretization

The finite element method is used to discretize the minimization problem [60]

$$\begin{cases} \underline{U}^{PFM} = \arg \left(\min_{\underline{U} \in V_{\underline{U}}^D(\Omega)} (\mathcal{E}_T^*) \right), \text{ with } \mathcal{E}_T^* = \mathcal{E}_s^* + \mathcal{E}_b^* \\ \partial_t \varphi \leq 0. \end{cases} \quad (6)$$

The time variable (i.e., incremental step since quasi-static fracture is considered) $t \in [0, T]$ is discretized in a sequence of time instants $\{t^k\}_{k \in \llbracket 1, N_T \rrbracket}$ with N_T defined as $t^{N_T} = T > 0$ being the final time. The time step size is defined for all $k \in \mathbb{N}$ as $\delta t = t^{k+1} - t^k > 0$.

The temporal derivative of the variable φ is approximated by the difference quotient

$$\forall k \in \mathbb{N}, \partial_t \varphi \approx \frac{\varphi(t^{k+1}) - \varphi(t^k)}{\delta t}. \quad (7)$$

Then, let us call $\{\underline{U}\}^k = \{(\underline{U}, \varphi)(\underline{x}_n, t^k)\}_{n \in [1, N_{nodes}]} \in V \times W$ the degrees of freedom at each node \underline{x}_n and instant $\{t^k\}_{k \in \llbracket 1, N_T \rrbracket}$ with $V = V_{\underline{U}}^D(\Omega)$ and $W = H^1(\Omega)$. The Hilbert space on the total domain Ω is denoted $H^1(\Omega) = \{\underline{U} \in L^2(\Omega) \mid \nabla \underline{U} \in L^2(\Omega)\}$.

The minimization problem (6) becomes

$$\forall k \in \mathbb{N}^* \begin{cases} \{\underline{U}^{PFM}\}^k = \arg \left(\min_{\{\underline{U}\}^k \in V \times W} (\mathcal{E}_T^* (\{\underline{U}\}^k)) \right) \text{ on } V \times W, \\ \{\underline{U}^{PFM}\}^k \leq \{\underline{U}^{PFM}\}^{k-1} \text{ on } 0 \times W. \end{cases} \quad (8)$$

Uniform mesh pre-refinement is utilized (Figure 5). This choice avoids the interaction with G_c and effective fracture toughness [13, 56, 64].

2.3 Nonlinear and linear numerical solutions

The numerical solution to Equation (8) is determined using a combined active set Newton primal-dual active set method in which the irreversibility constraint and nonlinearities in the system are treated simultaneously using a combined active set Newton method [26]. The linear equation systems are solved with a parallel matrix-free geometric multigrid method [34, 37], related to the solution

concepts designed in `pfm-cracks` [28], and based on the finite element library `deal.II` [4, 5]. Let us consider the following linear system at each Newton iteration $j \in \mathbb{N}^*$ and at each instant t^k

$$\forall k \in \mathbb{N} \begin{cases} \{\underline{U}^{PFM}\}_{j+1}^k = \{\underline{U}^{PFM}\}_j^k + \{\delta\underline{U}^{PFM}\}_j^k \\ \nabla^2 \mathcal{E}_T(\{\underline{U}^{PFM}\}_j^k) \{\delta\underline{U}^{PFM}\}_j^k = -\nabla \mathcal{E}_T(\{\underline{U}^{PFM}\}_j^k) \\ \{\delta\underline{U}^{PFM}\}_j^k \leq 0 \text{ on } 0 \times W. \end{cases} \quad (9)$$

The notations are simplified by dropping the indices k of time and j of the Newton iteration. Let us consider the operator G symmetric and positive as $\underline{G} = \nabla^2 \mathcal{E}_T(\{\underline{U}^{PFM}\}_j^k)$ and the operator $\underline{F} = -\nabla \mathcal{E}_T(\{\underline{U}^{PFM}\}_j^k)$. The minimization problem (9) is solved using a Lagrange multiplier $\lambda \in 0 \times W^*$ (with W^* the dual space of W) with a chosen value of $c > 0$

$$\begin{cases} \forall \{\underline{Z}\} \in V \times W, (\underline{G}\{\delta\underline{U}^{PFM}\}, \{\underline{Z}\}) + (\lambda, \{\underline{Z}\}) = (\underline{F}, \{\underline{Z}\}) \\ C(\{\delta\underline{U}^{PFM}\}, \lambda) = 0 \text{ on } 0 \times W \\ \text{with } C(\{\delta\underline{U}^{PFM}\}, \lambda) = \lambda - \max(0, \lambda + c\{\delta\underline{U}^{PFM}\}) \text{ on } 0 \times W. \end{cases} \quad (10)$$

For the primal-dual active set strategy, the condition $C(\{\delta\underline{U}^{PFM}\}, \lambda) = 0$ on $0 \times W$ in Equation (10) is replaced by $\{\delta\underline{U}^{PFM}\} = \{0\}$ when the \underline{x} position is in the active set domain \mathcal{A} and by $\lambda = 0$ in the inactive set domain \mathcal{I} . These domains are defined for Newton iteration $j \in \mathbb{N}^*$

$$\begin{cases} \text{Active set domain: } \mathcal{A}_j = \{\underline{x} \mid \lambda_j(\underline{x}) + c\{\delta\underline{U}^{PFM}\}_j(\underline{x}) > 0\} \\ \text{Inactive set domain: } \mathcal{I}_j = \{\underline{x} \mid \lambda_j(\underline{x}) + c\{\delta\underline{U}^{PFM}\}_j(\underline{x}) \leq 0\}. \end{cases} \quad (11)$$

The numerical solution consists in repeating for $j \in \mathbb{N}^*$ Equation (12) until there is no longer any change of the active set domain \mathcal{A}_j

$$\begin{cases} \forall \{\underline{Z}\} \in V \times W, (\underline{G}\{\delta\underline{U}^{PFM}\}_{j+1}, \{\underline{Z}\}) + (\lambda_{j+1}, \{\underline{Z}\}) = (\underline{F}, \{\underline{Z}\}) \\ \forall \mu \in 0 \times W, (\{\delta\underline{U}^{PFM}\}_{j+1}, \mu) = 0 \text{ on } \mathcal{A}_j \\ \lambda_{j+1} = 0 \text{ on } \mathcal{I}_j. \end{cases} \quad (12)$$

The derivation of the governing complementarity system resulting in Equations (10) and (12) is extensively described in Ref. [36].

3 Williams' series

This section provides details on Williams' series, which is the analytical solution of a conventional fracture mechanics problem [54]. A continuous medium Ω' in the complex plane is considered. The positions $\underline{z} \in \Omega'$ are written in the Cartesian $(x, y) \in \mathbb{R}^2$ or polar coordinate $(r, \theta) \in \mathbb{R}_+ \times [-\pi, +\pi]$ systems.

3.1 Model and hypothesis

The material model and hypotheses are the same as in Ref. [54]. The medium Ω' is considered as an infinite plate in the complex plane except in the cracked region $\mathcal{C}' = \{\underline{z} = x+iy \in \mathbb{C}, x \in [-a, 0], y = 0\}$

with $a \in \mathbb{R}_+$ being the length of the crack. The material is isotropic linear elastic in $\Omega' = \mathbb{C} \setminus \mathcal{C}'$. The origin of the coordinate system ($\underline{z} = \underline{0}$) is at the tip of the crack, which propagates along a straight path. The displacement field, defined for $\underline{z} \in \Omega'$, reads $\underline{U}(\underline{z}) = U_x(\underline{z}) + iU_y(\underline{z}) \in \mathbb{C}$. The (i, j) components of the stress tensor $\underline{\sigma} \in \mathbb{R}^{2 \times 2}$ are σ_{ij} , and are also defined for $\underline{z} \in \Omega'$. Because the material is considered as linear elastic, the fields \underline{U} and $(\sigma_{ij})_{i,j=x \text{ or } y}$ are holomorphic in Ω' .

The medium is considered to be remotely controlled by uniaxial tension σ_{yy}^∞ and in-plane shear loading σ_{xy}^∞ such that

$$\lim_{|\underline{z}| \rightarrow +\infty} \sigma_{yy}(\underline{z}) = \sigma_{yy}^\infty; \quad \lim_{|\underline{z}| \rightarrow +\infty} \sigma_{xy}(\underline{z}) = \sigma_{xy}^\infty; \quad \lim_{|\underline{z}| \rightarrow +\infty} \sigma_{xx}(\underline{z}) = 0. \quad (13)$$

Moreover, traction-free boundaries are assumed in the region of the crack \mathcal{C}'

$$\forall \underline{z}^\pm \in \Omega' \text{ with } x < 0 \text{ and } y \rightarrow \pm 0, \quad \sigma_{xy}(\underline{z}^\pm) = \sigma_{yy}(\underline{z}^\pm) = 0. \quad (14)$$

3.2 Definition of Williams' series

Williams' series [61] are based on the stress and displacement fields derived from the Muskhelishvili and Kolosov potentials [49] in 2D elasticity. Williams' displacement field \underline{U}^{WS} is written as

$$\forall \underline{z} \in \Omega', \quad \underline{U}^{WS}(\underline{z}) = \sum_{n=N_0}^{N_1} [\gamma_n^I \cdot \underline{\Gamma}_n^I(\underline{z}) + \gamma_n^{II} \cdot \underline{\Gamma}_n^{II}(\underline{z})], \quad (15)$$

where, $N_0 \in \mathbb{Z}$ and $N_1 \in \mathbb{N}$ are the minimum and maximum orders that are taken into account for truncated series. The influence of the chosen values is discussed in Section 3.3. The coefficients $\{\gamma_n^I\}_{n \in \llbracket N_0, N_1 \rrbracket}$ and $\{\gamma_n^{II}\}_{n \in \llbracket N_0, N_1 \rrbracket}$ are called Williams' series amplitudes, respectively in modes I and II. The unitary displacement fields $\underline{\Gamma}_n^I$ and $\underline{\Gamma}_n^{II}$ corresponding to modes I and II, respectively, are defined at order $n \in \mathbb{Z}$ by

$$\forall \underline{z} \in \Omega', \quad \begin{cases} \underline{\Gamma}_n^I(\underline{z}) = \frac{r^{n/2}}{2\mu\sqrt{2\pi}} \left(\kappa e^{\frac{i\theta n}{2}} - \frac{n}{2} e^{i\theta(2-\frac{n}{2})} + \left(\frac{n}{2} + (-1)^n\right) e^{-\frac{i n \theta}{2}} \right), \\ \underline{\Gamma}_n^{II}(\underline{z}) = \frac{i r^{n/2}}{2\mu\sqrt{2\pi}} \left(\kappa e^{\frac{i\theta n}{2}} + \frac{n}{2} e^{i\theta(2-\frac{n}{2})} + \left(-\frac{n}{2} + (-1)^n\right) e^{-\frac{i n \theta}{2}} \right), \end{cases} \quad (16)$$

where $\mu > 0$ is the shear modulus of the undamaged material, and κ Kolosov's parameter. Considering plane strain conditions, the latter becomes $\kappa = 3 - 4\nu$.

3.3 Extraction of fracture mechanics parameters from Williams' series

Let us consider a pure mode I crack propagation case. The displacement fields are called ‘‘supersingular’’ when $n < 0$ [24], and ‘‘subsingular’’ when $n \geq 0$. The ‘‘supersingular’’ fields are of interest in the present analysis. More specifically, let us focus on the case $n = -1$. To avoid a singularity of the elastic energy at $\underline{z} = \underline{0}$, the displacement field at order $n = -1$ should reduce to zero provided the crack tip is correctly positioned [24, 29]. Otherwise, it leads to a crack tip shift da defined from Williams' amplitudes γ_{-1}^I and γ_1^I as

$$da = -2 \frac{\gamma_{-1}^I}{\gamma_1^I}. \quad (17)$$

The extent (i.e., diameter) of the Fracture Process Zone (FPZ) is proportional to

$$d_{FPZ}^2 = -8 \frac{\gamma_1^I}{\gamma_1^I}. \quad (18)$$

Last, the Stress Intensity Factors (SIFs) in modes I and II are obtained by

$$K_I = \gamma_1^I \in \mathbb{R}^+, \quad (19)$$

$$K_{II} = \gamma_1^{II} \in \mathbb{R}. \quad (20)$$

The energy release rate $\mathcal{G} \geq 0$ is determined from K_I and K_{II} in plane strain hypothesis as

$$\mathcal{G} = (1 - \nu^2) \frac{K_I^2 + K_{II}^2}{E}. \quad (21)$$

4 Post-processing phase-field displacement fields by Williams' series

Phase-field models provide a regularized description of the development of damage in quasi-brittle materials. Such a continuous description offers a numerical framework that can be merged into the finite element method, and models quite well the fracture process zone observed experimentally in such materials. Conversely, fracture mechanics explicitly describes displacement discontinuities observed during crack propagation. The discontinuous description generally ignores the fracture process zone. It is proposed to search for a kinematic equivalence between both analyses to provide the crack tip positions for phase-field results in addition to equivalent fracture mechanics parameters.

4.1 Crack tip position

The phase-field displacement fields (Section 2) are post-processed via Williams' series (Section 3) first to determine the crack tip position. Two superimposed geometries are used (Figure 2). The first one, Ω , is the structure of interest arbitrarily chosen by the user, with corresponding boundary conditions and material behavior. The phase-field model is applied to compute the phase-field variable and the displacement field in Ω . The second geometry with internal and external diameters d_i and d_e , respectively, is called "pacman". It belongs to the domain Ω' defined in Section 3. It is chosen as a consequence of Williams' fields that are defined in polar coordinates (Section 3). The inner diameter d_i is such that the "mouth" of the pacman excludes both the crack and the fracture process zone. The crack tip corresponds to the center of the pacman.

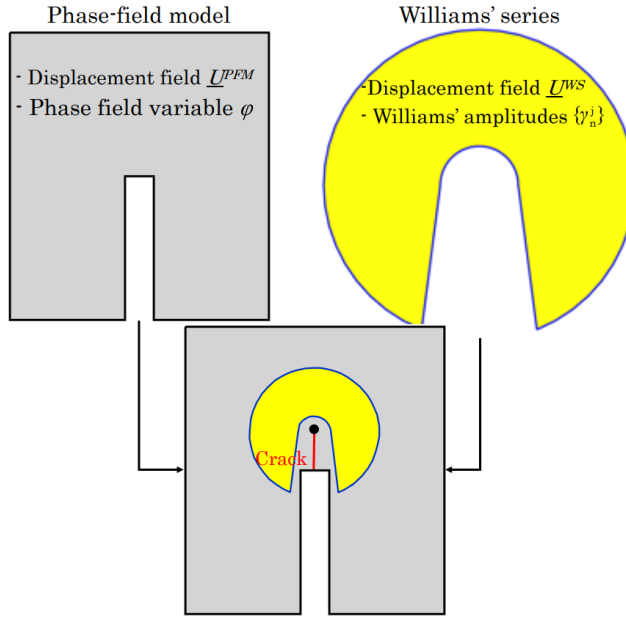


Figure 2: Domain for post-processing phase-field simulations using Williams' series to determine fracture mechanics parameters

Figure 3 gives an overview of the post-processing algorithm. The method starts with the phase-field analysis of the structure of interest, which is solved for the whole time-space domain $\Omega \times (0, T)$. The distribution of the phase-field variable φ at the final time T is used to determine the inner diameter d_i of the pacman such that its domain does not contain the phase-field region where $\varphi > 0.5$ for any time step (first assumption of the size of the FPZ). Once the pacman geometry has been defined, the mesh for Williams' series is generated and kept identical for the whole analyses.

The identification procedure begins by placing the pacman where the crack is expected to initiate (e.g., for a notched beam, centering the pacman around the root of the notch). During the loading history, the fracture process zone grows away from the initial notch. Consequently, the position of the equivalent crack tip has to be determined and the pacman is moved. Knowing the crack tip location for time t_k , a loop aims to determine the crack tip location for time t_{k+1} (inner dashed rectangle in Figure 3). It first calculates Williams' amplitudes $\{\gamma_n^I\}_{n \in \llbracket N_0, N_1 \rrbracket}^k$ (mode I) and $\{\gamma_n^{II}\}_{n \in \llbracket N_0, N_1 \rrbracket}^k$ (mode II) via least squares minimization between Williams' displacement field \underline{U}^{WS} and that from the phase-field model \underline{U}^{PFM} . From these amplitudes, the crack tip shift da_j is estimated (Equation 17), the pacman position is updated, and the process is iterated until the absolute value of da_j becomes less than da_{lim}

$$a(t_{k+1}) = a(t_k) + \sum_{j=1}^m da_j \text{ with } da_m < da_{lim}. \quad (22)$$

The value of the critical crack tip shift da_{lim} is chosen to be equal to $0.2h_{\min}^W$, with h_{\min}^W the minimum element size of the pacman mesh. Thus, contrary to Ref. [56], the algorithm iteratively tracks the crack tip and translates the pacman to ensure that it is centered about the crack tip at each time step. Once convergence has been reached for time t_k , the tip position is determined for the following time t_{k+1} through the iterative loop illustrated by the external dashed rectangle in Figure 3.

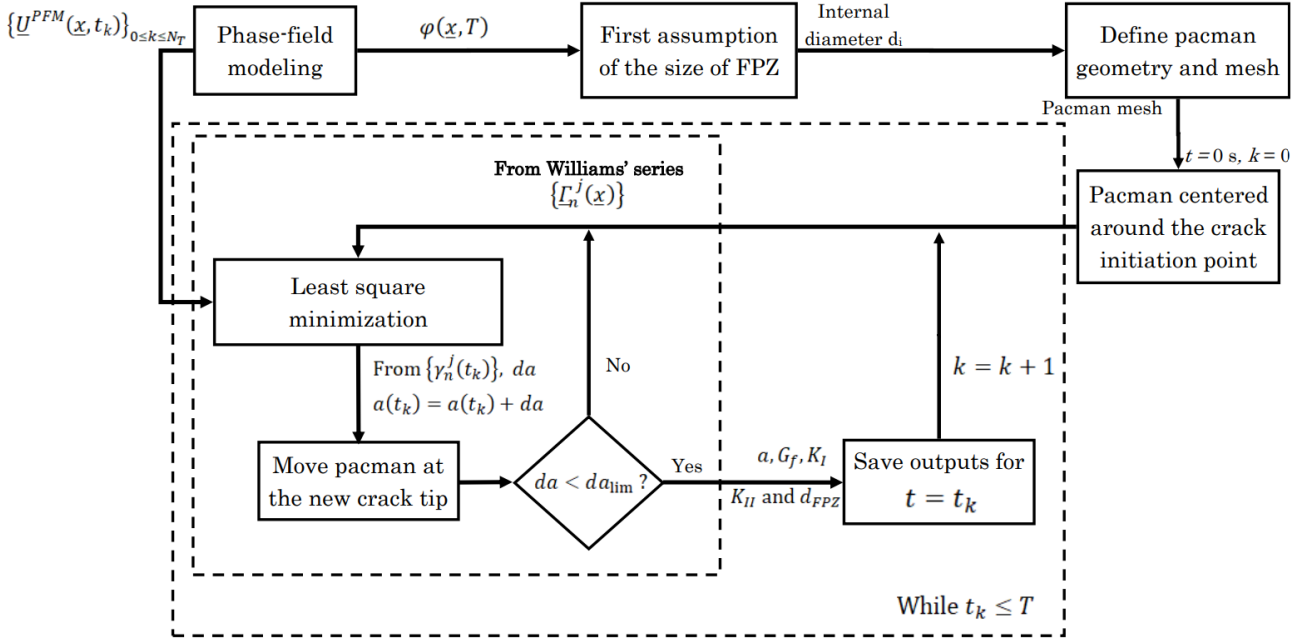


Figure 3: Workflow of the global algorithm

4.2 Equivalent fracture mechanics parameters

Knowing the crack tip location and the associated Williams' series for any time step, the equivalent fracture mechanics parameters, namely, the energy release rate \mathcal{G} , the stress intensity factors K_I and K_{II} and the size of the fracture process zone d_{FPZ} (Equation 18) are identified for any given time step. It is worth noting that the present goal is not identifying the parameters used for the phase-field model [38], but to extract equivalent fracture mechanics parameters. Further, the way the energy is dissipated is different in both approaches [42]. Volume dissipation occurs using phase-field models. Conversely, surface dissipation associated with the creation of new surfaces along the crack is accounted for in fracture mechanics.

5 Application to a notched beam

The post-processing procedure (Section 4) is applied to a two-dimensional case, namely, a beam with controlled notch opening displacement inspired by the crack tip opening displacement (CTOD) and crack mouth opening displacement (CMOD) of three-point flexural tests on notched beams [6]. The geometry of the beam is shown in Figure 4. The crack propagates by prescribing the Notch Opening Displacement (NOD) δ between points A and B , i.e., the Dirichlet boundary conditions are chosen as $\underline{U}_D(A, t) = -\delta(t)\underline{x}/2$ and $\underline{U}_D(B, t) = \delta(t)\underline{x}/2$ with a constant speed $\dot{\delta} = 3 \mu\text{m/s}$. To cancel out rigid body motions, the displacement of point C is equal to 0, namely, the Dirichlet condition $\underline{U}_D(C, t) = \underline{0}$. Mathematically, the prescription of point values in a two-dimensional domain requires sufficient regularity of the domain and the solution functions.

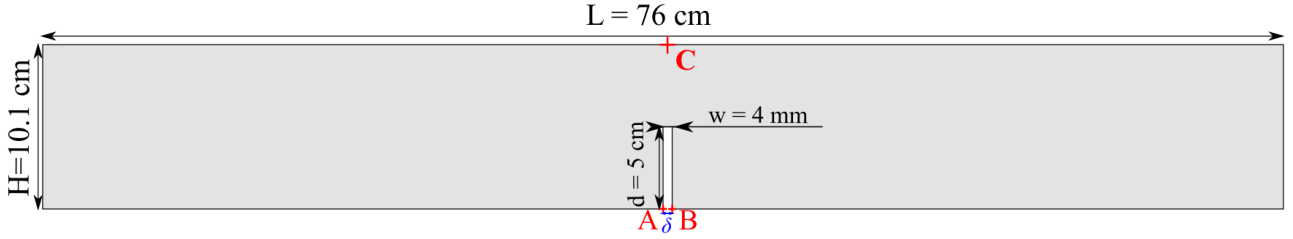


Figure 4: Geometry of the beam, notch opening displacement δ between points A and B . The simulations are run in a two-dimensional setting accounting for a constant thickness of $W = 100$ mm in the third dimension

The phase-field solutions are computed following Ref. [37]. Williams' series are evaluated using the `Correli 3.0` library [41]. The data are exchanged between the two codes via Matlab scripts.

5.1 Phase-field simulations

The displacement fields for parameter identification, which is performed in Section 6, are delivered by finite element simulations to solve the aforementioned phase-field model for brittle fracture. The computations are performed on 5 different meshes, which are created by globally pre-refining an initial mesh 2, 3, 4, 5 and 6 times. The number of global pre-refinements is denoted by N_{ref} , and the corresponding meshes are displayed in Figure 5. The phase-field material parameters are gathered in Table 1, and the numerical parameters in Table 2. The minimum element size h_{min} describes the minimum diagonal diameter over all elements of the mesh.

Table 1: Mechanical parameters of the notched beam

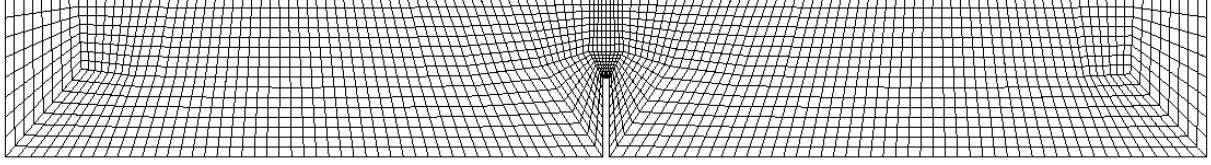
Parameter	Value
Young's modulus, E	21 GPa
Poisson's ratio, ν	0.22
Critical energy release rate, \mathcal{G}_c	25 J/m ²

For rigorous computational convergence studies, the internal length ℓ_φ is usually chosen dependent on h_{min} to satisfy Γ -convergence [2, 3, 14], see also a closely related work on image segmentation [10, Section 3], and for phase-field fracture studies, the reader is referred to Refs. [26, 59, 60, 35]. In the present case, $\ell_\varphi = 16 h_{min}$, thus a unique relationship between ℓ_φ and h_{min} was prescribed. Such dependence with factors, for instance, 2, 4, or 16 as here, is enforced in most published studies using phase-field methods. This choice is made for phase-field fracture, but also phase-field methods used in multiphase flow or material sciences (see references cited in Ref. [60, Section 5.5, Remark 40]).

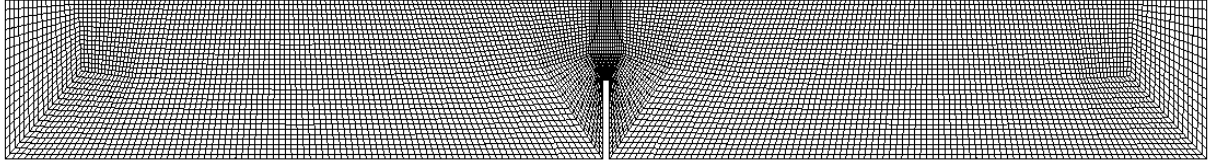
Table 2: Numerical parameters for the phase-field simulations using five different meshes (Figure 5)

Parameter	Value
Minimum element size, h_{\min}	[2.3, 1.1, 0.55, 0.27, 0.14] mm
Internal length, ℓ_{φ}	[36, 18, 8.8, 4.4, 2.2] mm
Bulk regularization parameter, ξ	[2.3, 1.1, 0.55, 0.27, 0.14] $\times 10^{-10}$
Newton lower bound, ρ_{cr}	10^{-6}
Maximum number of Newton iterations, N_{it}^{\max}	50
Time step size, δt	10 ms

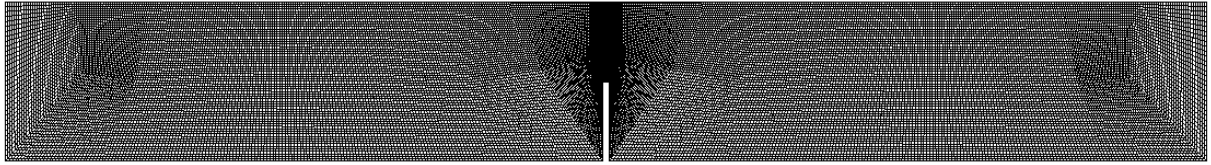
As incremental step size δt for the quasi-static simulations, $\delta t = 10$ ms is chosen. Larger and smaller time step sizes were also tested (Figure 15). The chosen one yielded the best results in terms of accuracy and computation time.



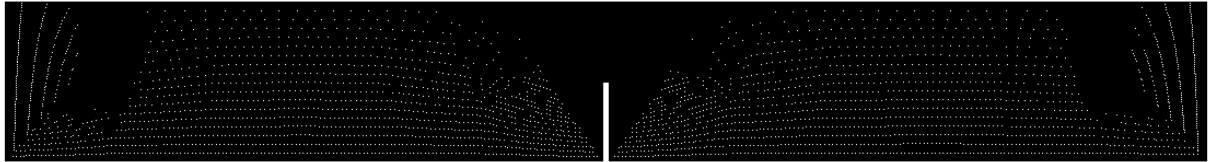
(a) $N_{DOF} = 4,370 + 2,185 = 6,555$; $h_{\min} = 2.3$ mm



(b) $N_{DOF} = 16,930 + 8,465 = 25,395$; $h_{\min} = 1.1$ mm



(c) $N_{DOF} = 66,626 + 33,313 = 99,939$; $h_{\min} = 0.55$ mm



(d) $N_{DOF} = 264,322 + 132,161 = 396,483$; $h_{\min} = 0.27$ mm



(e) $N_{DOF} = 1,052,930 + 526,465 = 1,579,395$; $h_{\min} = 0.14$ mm

Figure 5: Beam meshes with (a) $N_{ref} = 2$, (b) $N_{ref} = 3$, (c) $N_{ref} = 4$, (d) $N_{ref} = 5$ and (e) $N_{ref} = 6$. The total number of degrees of freedom N_{DOF} of the finite element simulation is composed of the degrees of freedom for the displacement and the phase-field variable. Since the displacement is a 2-dimensional field, there are 2 DOFs per displacement node, and 1 DOF per phase-field node

Figure 6 shows the phase-field variable φ when $t = 50$ s (i.e., for an NOD of $150 \mu\text{m}$) for the different meshes. The coarser the mesh, the larger the internal length ℓ_φ due to the dependence on h_{\min} . A larger internal length ℓ_φ leads to a more smeared damaged zone since the transition from fracture to the non-broken material is larger. This is due to the gradient term inside the Ambrosio-Tortorelli regularization functional [2, 3] as for bigger ℓ_φ this term dominates. These results show a slightly asymmetric distribution of the phase-field variable concerning the y -direction, which implies some asymmetries in the global results, such as for the displacement field in the x -direction (Figure 7). This is the reason for working in the full domain, rather than considering one half-beam only. However, these asymmetries are sufficiently small to assume the hypothesis of vertical crack propagation as a straight line in the y -direction.

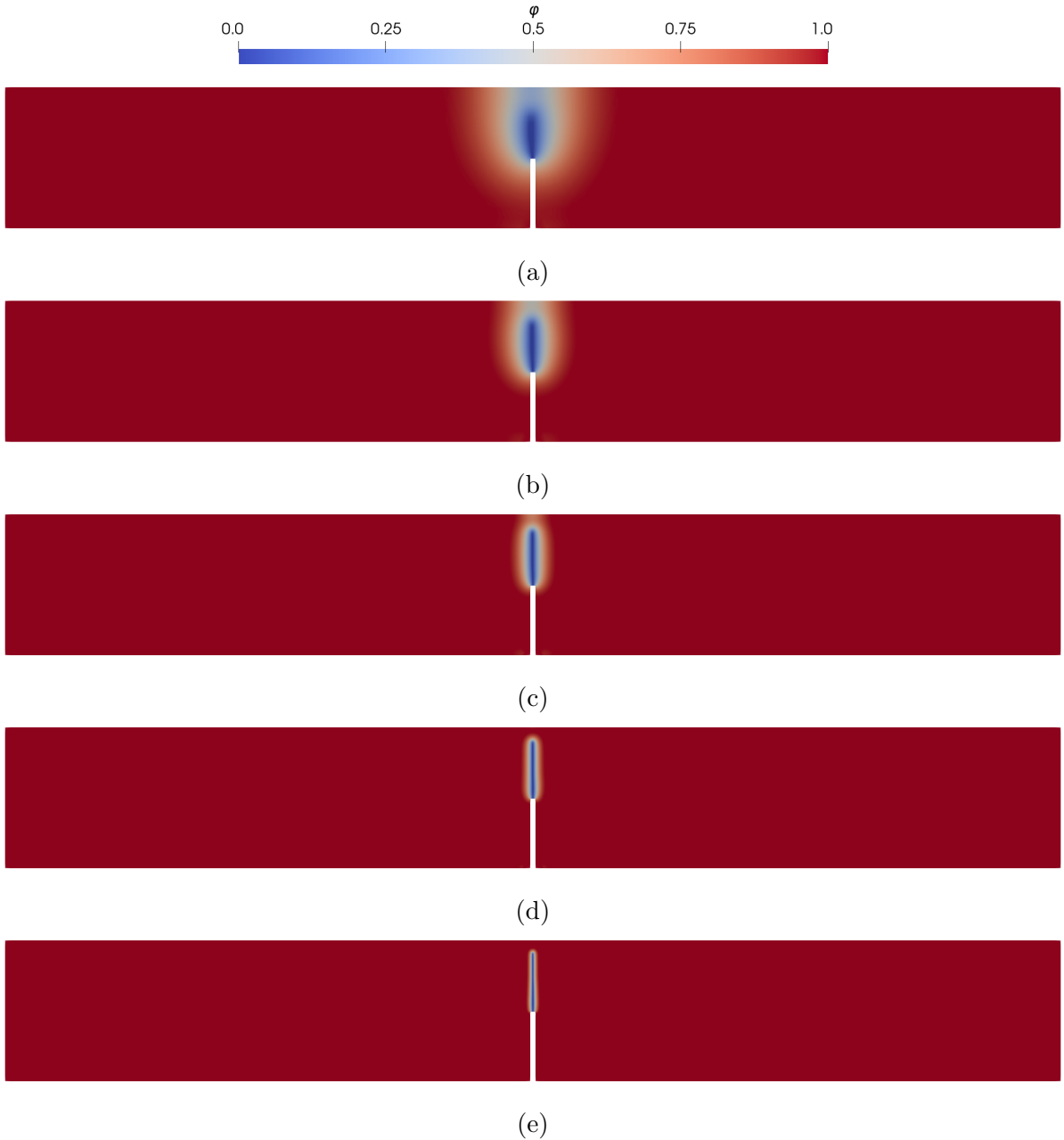


Figure 6: Phase-field variable φ field for an NOD of $150 \mu\text{m}$ for the meshes with various global refinements (Figure 5). (a) $N_{ref} = 2$, (b) $N_{ref} = 3$, (c) $N_{ref} = 4$, (d) $N_{ref} = 5$ and (e) $N_{ref} = 6$

Figure 7 shows the displacement field in the x -direction after 50 s of loading (i.e., an NOD of $150 \mu\text{m}$) for $N_{ref} = 5$. Very steep displacement gradients appear in one line of elements regardless of the choice of N_{ref} . The localization of the displacement field is a consequence of the choice of a very small bulk regularization parameter ξ [33]. The effect of this parameter on the final output will be studied in Section 5.3.4.

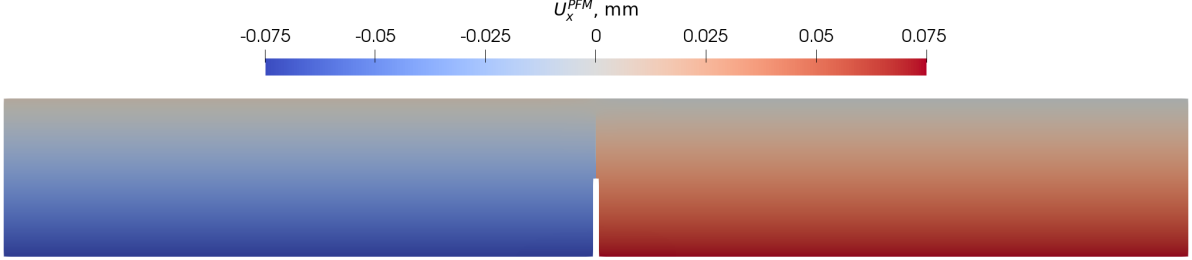


Figure 7: Horizontal displacement field U_x in the beam for an NOD of $150 \mu\text{m}$ and $N_{ref} = 5$

Figure 8 shows the change of the reaction force, which is obtained by evaluating the weak-form gradient \underline{F} (defined in Section 2.3) of the AT-1 energy functional (i.e., the so-called residual of the coupled variational inequality system) by setting the test function to zero everywhere; except on those Dirichlet boundaries, where one wants to evaluate the reaction forces. Consequently, as only two point values were considered as Dirichlet nodes, the test function is set to one there and zero otherwise. The ultimate levels are close for the different meshes. However, the higher the number of mesh refinements, the more brittle the overall response. This trend is due to the fact that the internal length ℓ_φ decreases and the brittle fracture Γ -limit is approached [11, 13].

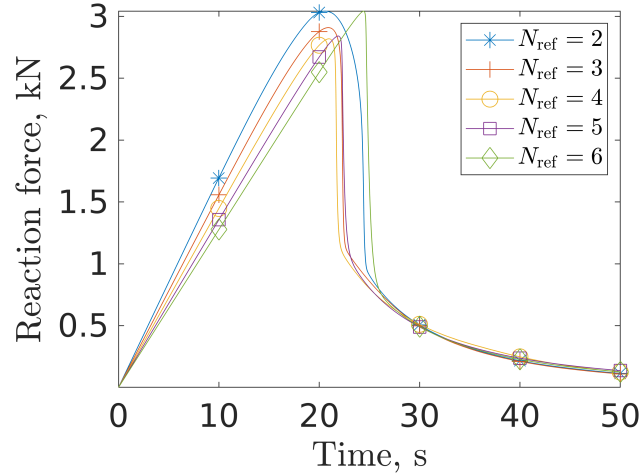


Figure 8: Reaction forces for different global refinement levels (for a beam width $W = 100 \text{ mm}$)

5.2 Pacman meshes

Williams' displacement fields are calculated on pacmen, which exclude the damaged region around the crack path. Each pacman is thus defined by an outer radius r_e and an inner radius r_i . Figure 9 shows different pacman geometries with the corresponding meshes on which Williams' series are computed depending on the value of ℓ_φ . The value of $r_e = 30 \text{ mm}$ is chosen to obtain an area of the pacman

large enough to encompass the fracture process zone for the largest internal length but not too large to avoid the edge of the beam as much as possible (see Section 5.3).

The inner radius is chosen according to the value of ℓ_φ such that the domain covered by the pacman is always associated with a phase-field level $\varphi \geq 0.5$. Therefore, the contour $\varphi = 0.5$ is determined at the last time step for each internal length. The value of r_i corresponds to the smallest inner radius for which the contour lies outside of the pacman. The change of the radius r_i with ℓ_φ is shown in Figure 9(e). The dependence of r_i with ℓ_φ (Figure 9(e)) is approximated by a least-squares regression leading to a coefficient of determination $R^2 = 0.991$, which indicates that an affine approximation is consistent. The slope of the linear regression is 0.49. Thus, setting $r_i = \ell_\varphi/2$ as the inner radius turns out to be a very good choice. This observation is justified by the choice of the elliptic regularization functionals [2, 3].

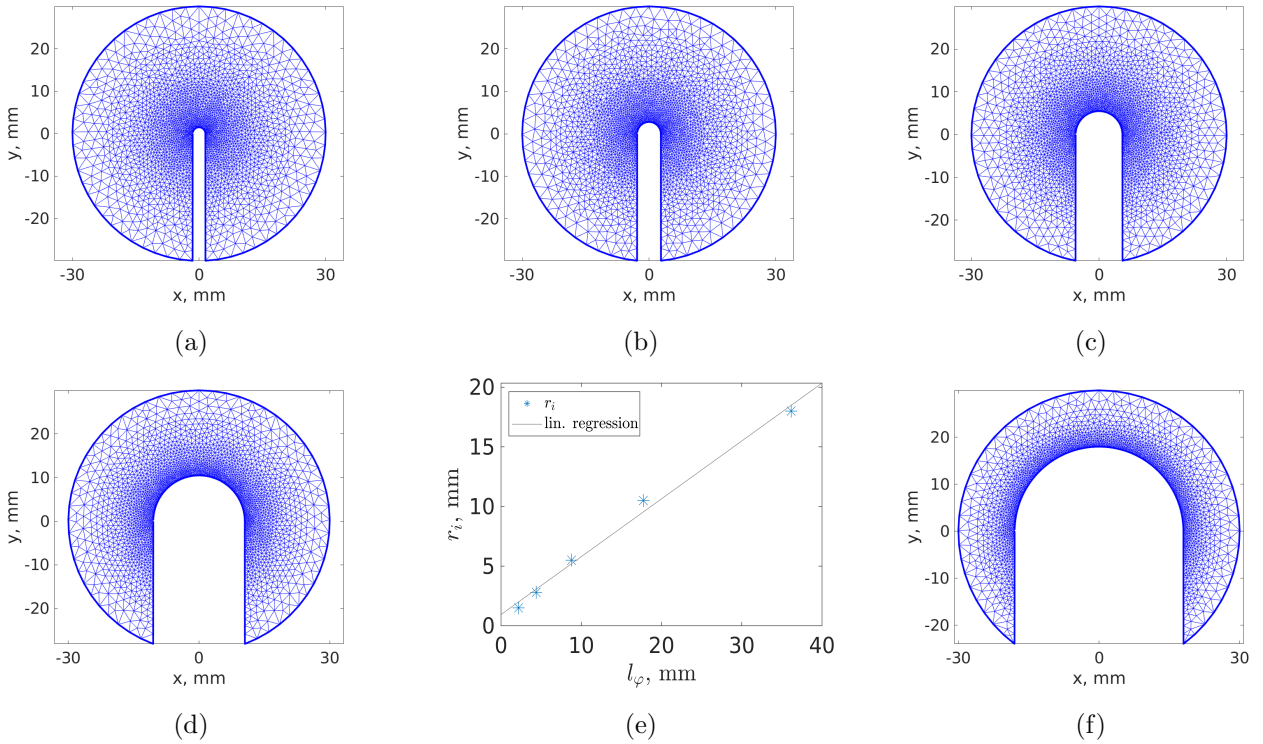


Figure 9: Pacman geometry and mesh adapted to the phase-field internal length ℓ_φ . (a) Pacman 1; (b) Pacman 2; (c) Pacman 3; (d) Pacman 4; (f) Pacman 5. (e) Evolution of the inner radius of the pacman with the value of the internal length ℓ_φ

The pacman mesh parameters (length scale, diameter, number of nodes, mean value of h , and minimal value of h) are provided in Table 3 once the inner radius was determined (Figure 9(e)). Even though the inner radius is significantly different for the five pacmen, the number of nodes to evaluate Williams' series and the mean element size are of the same order of magnitude.

Table 3: Pacman mesh parameters. The inner radius r_i is adapted to the value of ℓ_φ . N_{nodes} denotes the number of nodes, h_{mean}^W and h_{min}^W the mean and minimum element sizes, respectively. For triangular elements, their size corresponds to the diameter of the circumscribed circle

Pacman #	1	2	3	4	5
ℓ_φ , mm	2.2	4.4	8.8	18	36
r_i , mm	1.5	2.8	5.5	10.5	18
N_{nodes}	2,608	2,735	2,886	2,815	2,373
h_{mean}^W , mm	1.3	1.2	1.2	1.1	0.9
h_{min}^W , μm	240	255	280	275	260

5.3 Convergence of Williams' series applied to the phase-field solution

Using the fracture mechanics solution via Williams' series requires choosing specific subsingular and supersingular displacement fields. The values of the minimum and maximum orders are denoted by N_0 and N_1 (Equation (16)). Figures 10 and 11 show the difference fields of respectively $|U_x^{WS} - U_x^{PFM}|$ and $|U_y^{WS} - U_y^{PFM}|$ when $N_0 = -3$, $N_1 = 9$ for various time instants. These residuals are globally very low compared to the amplitudes of phase-field displacements that reach up to 75 μm for the displacement component in the x -direction (Figure 7).

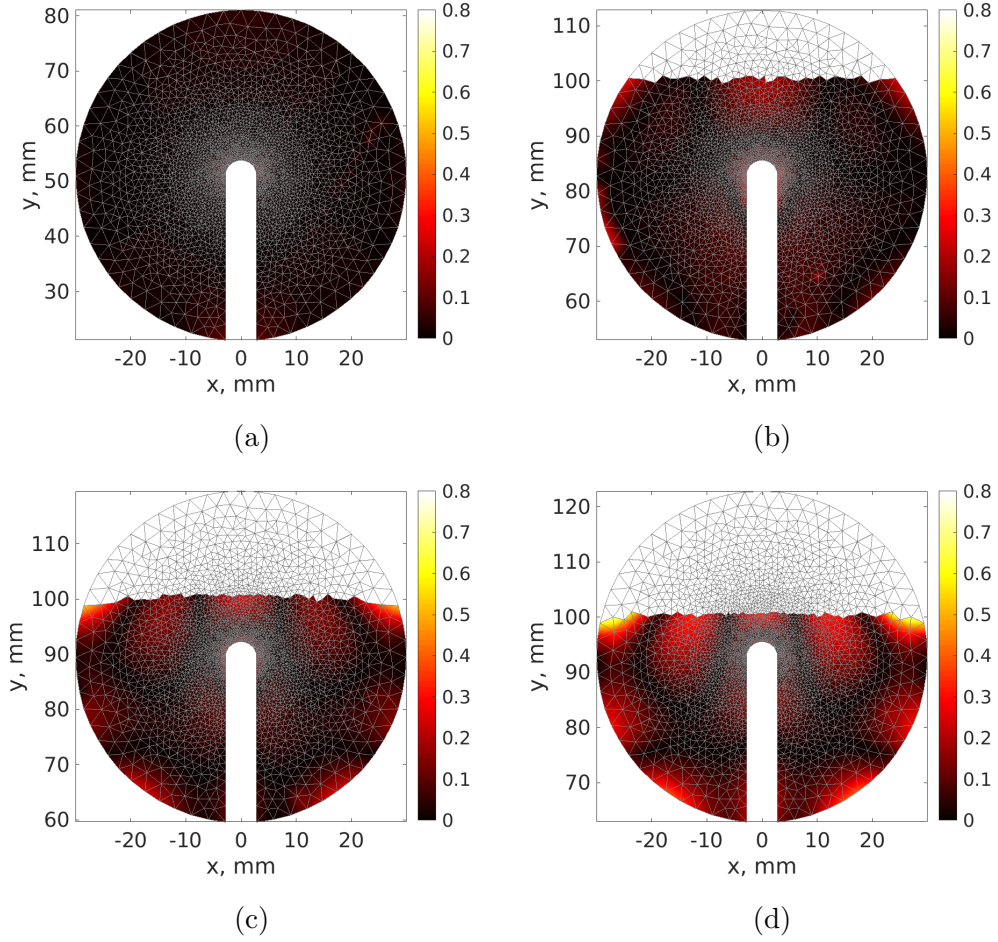


Figure 10: Residuals $|U_x^{WS} - U_x^{PFM}|$ expressed in μm between the displacement fields in the x -direction U_x^{WS} from Williams' series ($N_0 = -3$, $N_1 = 9$, Pacman 2) and U_x^{PFM} from the phase-field model ($\ell_\varphi = 4.4$ mm and $N_{ref} = 5$). (a) $t = 15$ s, (b) $t = 30$ s, (c) $t = 40$ s and (d) $t = 50$ s

The pacman meshes are moved to the new crack tip location each time increment. Thus, the pacman reaches the top edge of the beam at approximately 30 s, and the part of the mesh with no results increases with time. Williams' series are defined for an infinite medium Ω' contrary to the phase-field model defined inside the beam Ω . The free-edge conditions of the phase-field simulation eventually lead to an increase in the residuals. However, they remain very small, thus the following analyses are deemed trustworthy.

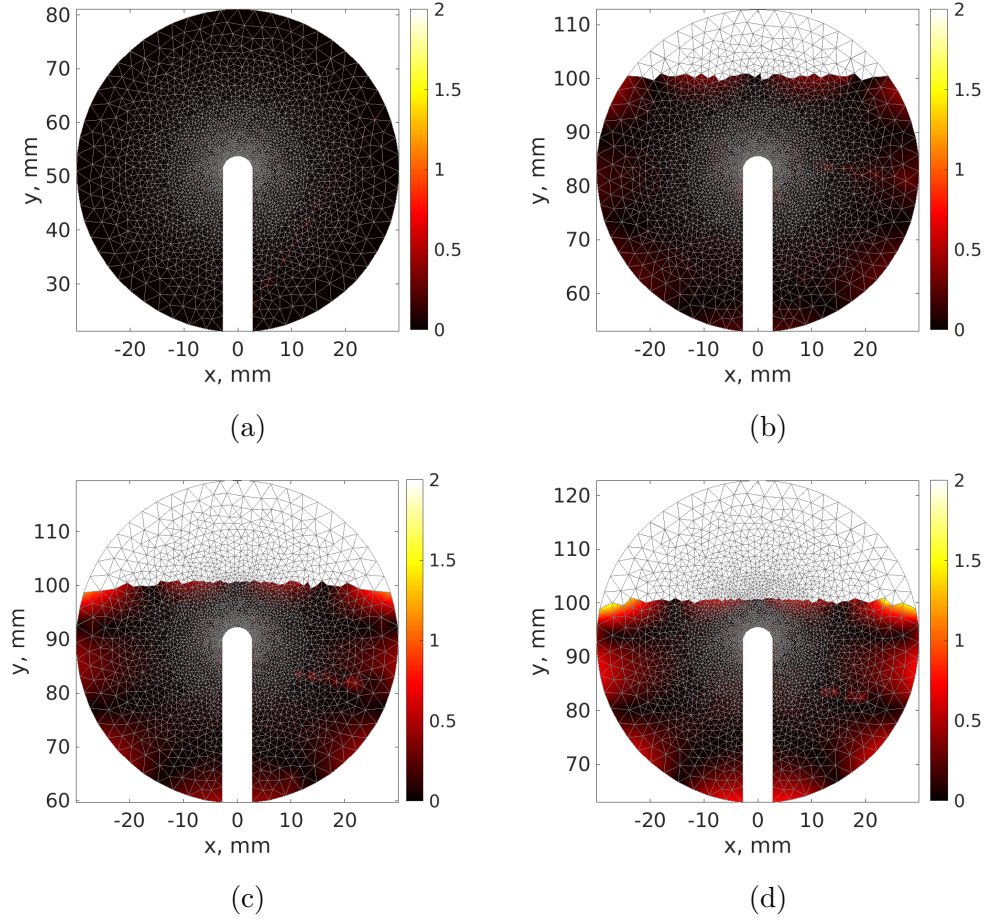


Figure 11: Residuals $|U_y^{WS} - U_y^{PFM}|$ expressed in μm between the displacement fields in the y -direction U_y^{WS} from Williams' series ($N_0 = -3$, $N_1 = 9$, Pacman 2) and U_y^{PFM} from the phase-field model ($\ell_\varphi = 4.4$ mm and $N_{ref} = 5$). (a) $t = 15$ s, (b) $t = 30$ s, (c) $t = 40$ s and (d) $t = 50$ s

5.3.1 Convergence of truncated Williams' series

Figure 12 shows different results at 50 s from the least squares minimization of Williams' series for the different quantities of interest. For the three investigated parameters, it is observed that convergence is ensured when $N_1 \geq 9$. Besides, given the mesh fineness, it is assumed that the choice $N_0 = -3$ is sufficient to get Williams' amplitude of order -3 to determine the size of the fracture process zone (Equation (18)). As a result, in the following, $N_0 = -3$ and $N_1 = 9$ are used.

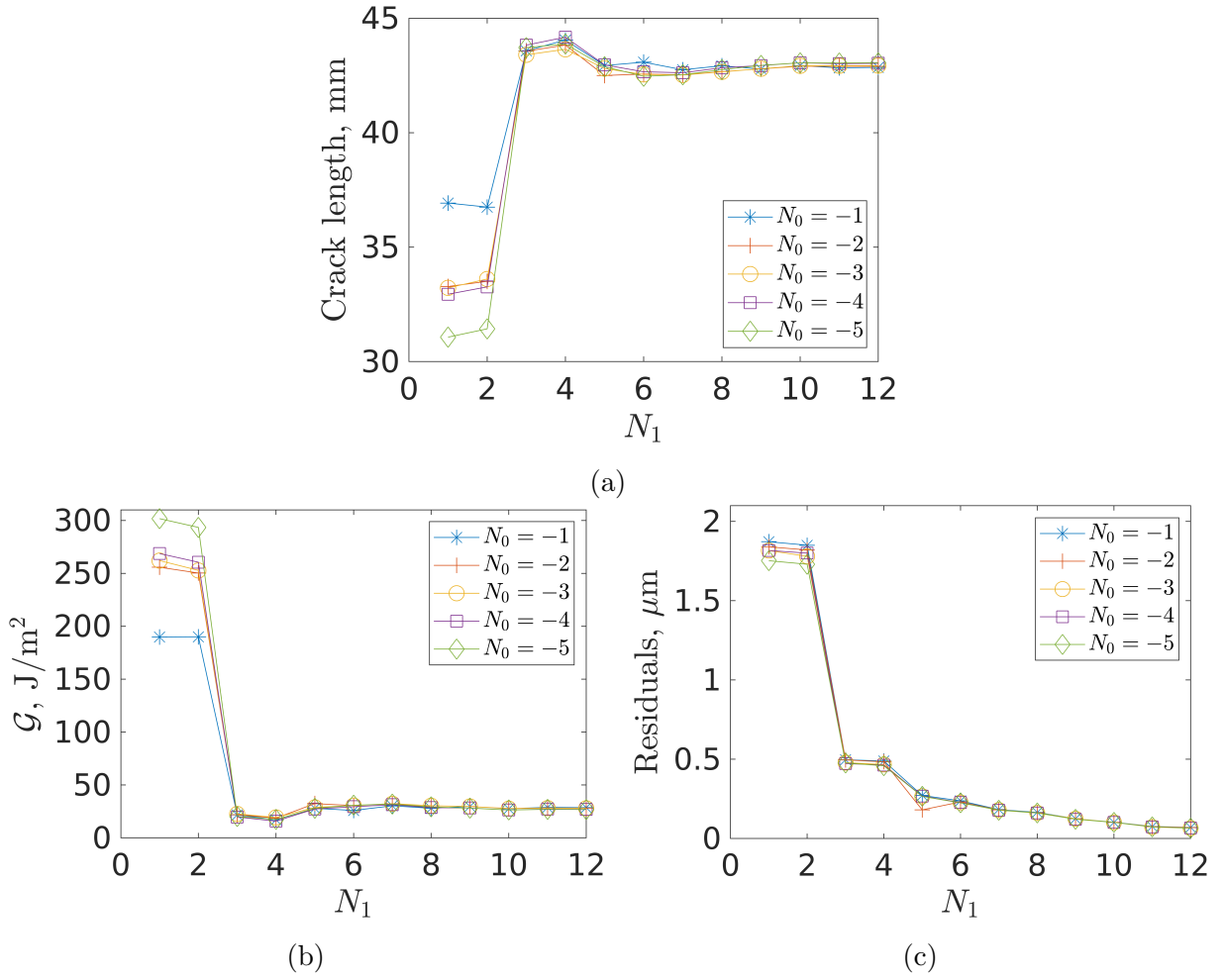


Figure 12: Fracture mechanics parameters identified between the phase-field displacement field ($\ell_\varphi = 4.4$ mm and $N_{ref} = 5$) and Williams' displacement fields at $t = 50$ s for different choices of N_0 and N_1 using Pacman 2 with Mesh M3 (Figure 13). (a) Crack length, (b) energy release rate and (c) RMS displacement residuals

5.3.2 Convergence with respect to the pacman mesh

The convergence with respect to the pacman discretization is studied for an inner radius $r_i = 2.8$ mm when $\ell_\varphi = 4.4$ mm (i.e., Pacman 2). Williams' displacement fields are constructed inside the pacman discretized with various meshes (i.e., M0, M1, M2 and M3) displayed in Figure 13, and whose characteristics are gathered in Table 4.

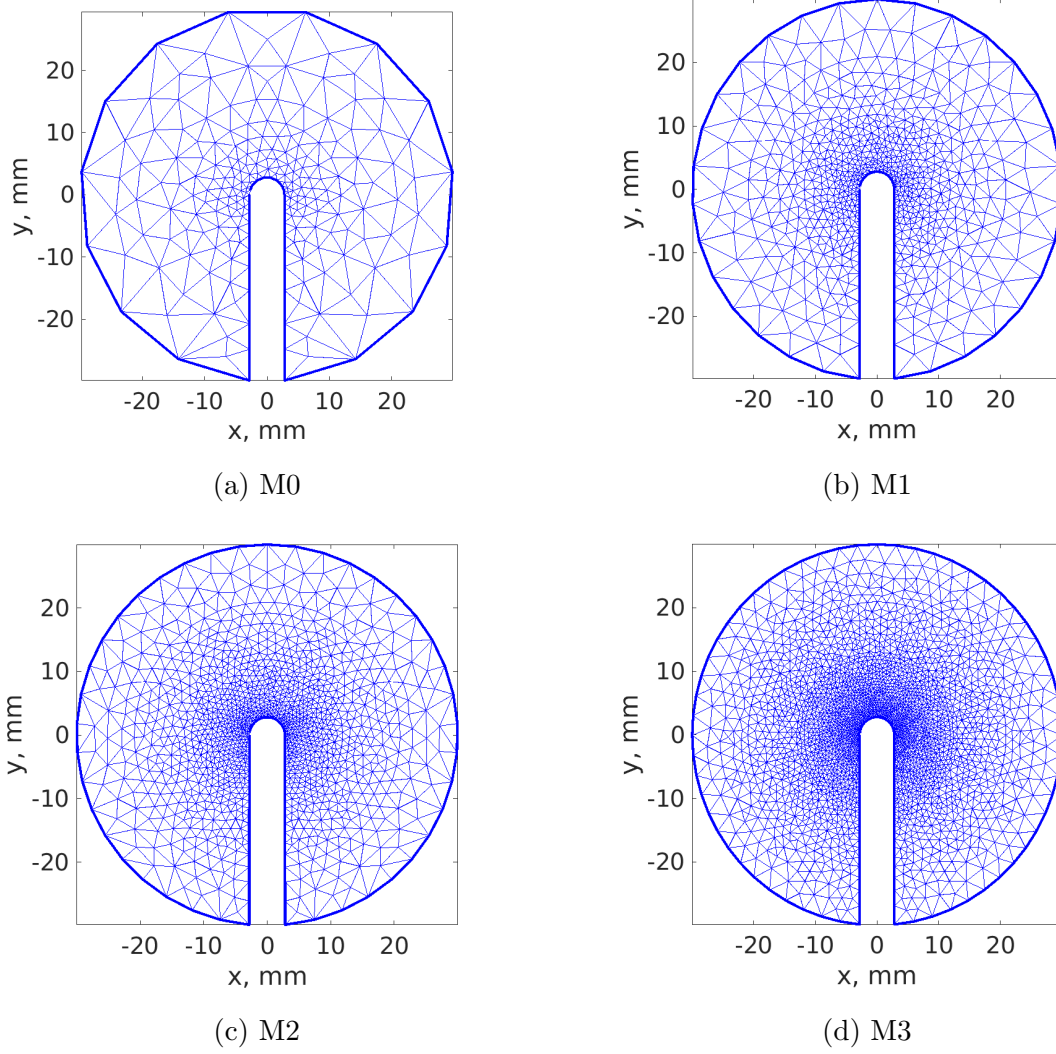


Figure 13: Meshes for convergence study for Pacman 2 ($r_i = 2.8$ mm and $r_e = 30$ mm)

Table 4: Mesh characteristics for convergence studies for Pacman 2, where N_{nodes} denotes the number of nodes, h_{mean}^W and h_{min}^W the mean and minimum sizes of elements, respectively. For triangular elements, their size corresponds to the diameter of the circumscribed circle

Mesh	M0	M1	M2	M3
N_{nodes}	222	722	1,324	2,735
h_{mean}^W , mm	4.5	2.4	1.8	1.2
h_{min}^W , μm	810	480	395	255

The influence of the mesh size of the pacman on the identification residuals, crack length, energy release rate, and the size of the Fracture Process Zone (FPZ) is shown in Figure 14. Only very small changes are observed. The RMS residuals (Figure 14(a)) have a level less than $0.15 \mu\text{m}$ at each time step for any choice of pacman mesh. After $t = 30$ s, the increase of the residuals is due to boundary effects (Figures 10 and 11). However, because these residuals did not degrade too much, the results after $t = 30$ s are still considered reliable. In the following parts, the calculations will be carried out

with the lowest possible residuals using the M3 discretization (Figure 13(d) and Table 4). It is worth noting that the mesh used in Figures 10 and 11 was also M3.

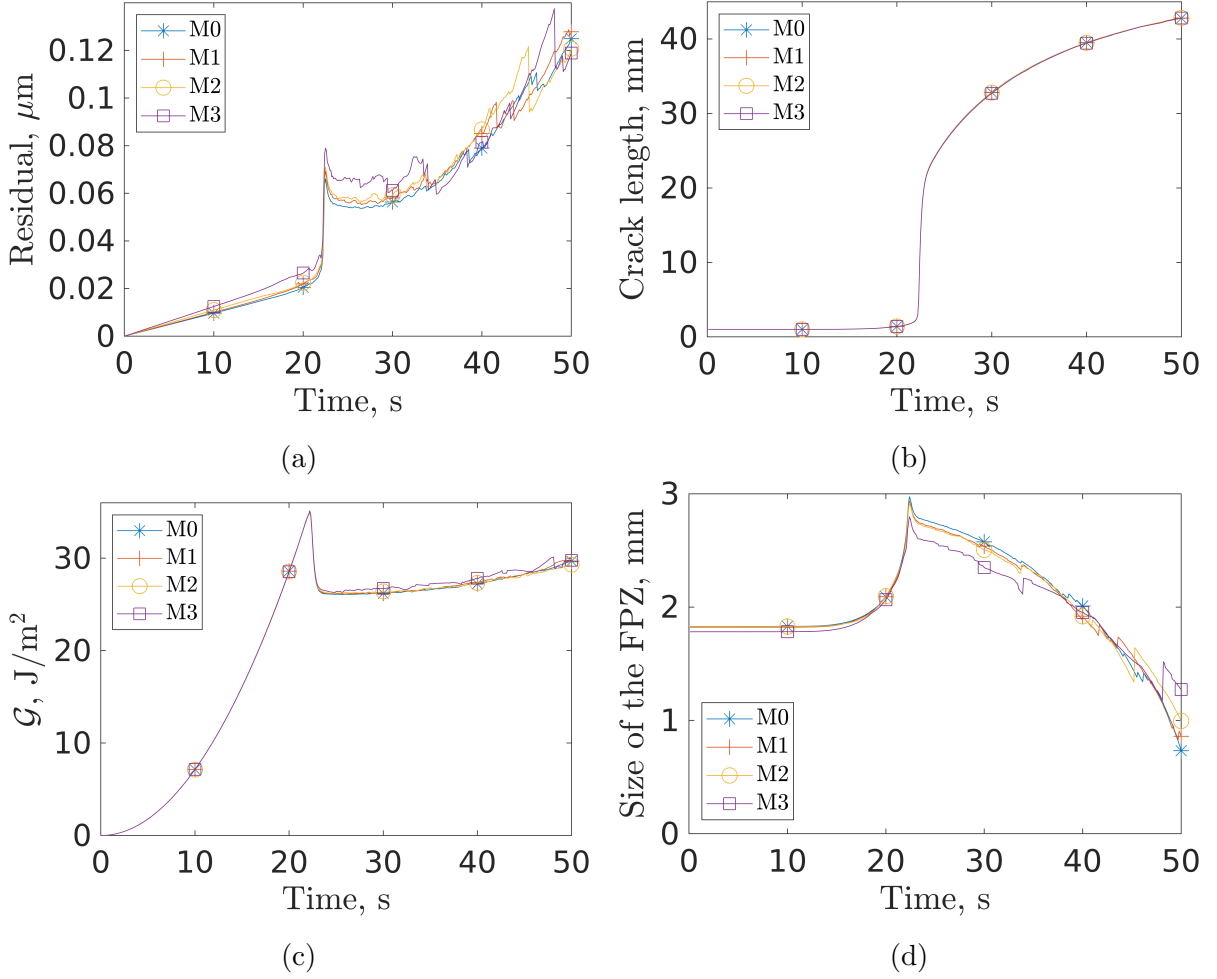


Figure 14: Fracture mechanics quantities determined from the phase-field model ($\ell_\varphi = 4.4$ mm and $N_{ref} = 5$) using Williams' series ($N_0 = -3$, $N_1 = 9$) with Pacman 2 and different meshes (Figure 13). (a) RMS displacement residuals, (b) crack length, (c) energy release rate, and (d) size of the fracture process zone (FPZ)

5.3.3 Influence of the time step size in the phase-field simulations

Figure 15 shows the histories of energy release rate \mathcal{G} (computed with Equation (21)) and mode I SIF K_I (Equation (19)) based on different time step sizes used for the phase-field simulations. All simulations are performed on the mesh and regularization parameters according to $N_{ref} = 5$. It is observed that the time step size of the simulation influences the results. If the time step size is chosen too large, the simulation fails in representing the brittleness of the material. Conversely, very small time step sizes lead to unrealistic peaks when propagation starts. Additionally, the amount of data and computation time become very large. The choice $\delta t = 10$ ms yields satisfying results while keeping the computational expense on a reasonable level. Thus, all the following results are based on $\delta t = 10$ ms.

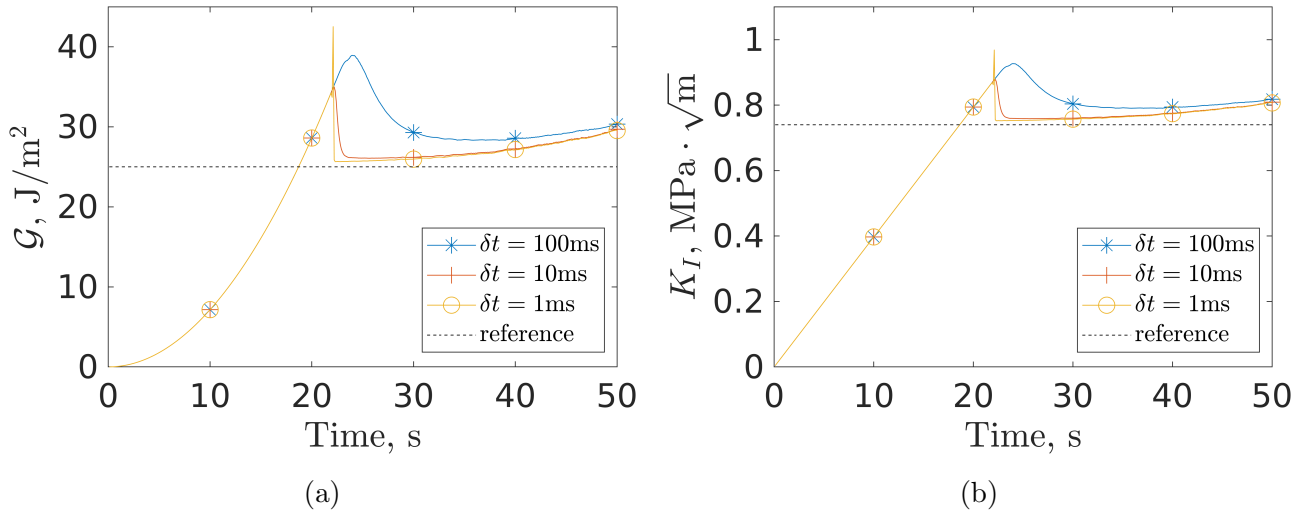


Figure 15: Identification of the energy release rate (a) and mode I stress intensity factor (b) for different time step sizes of the finite element simulations with $N_{ref} = 5$

5.3.4 Influence of the bulk regularization parameter

The parameter ξ regularizes the bulk energy (Equation (4)) and influences the phase-field displacements in the vicinity of the crack mouth. A very steep gradient of the displacements in the x -direction along the crack path is observed for $\xi = 10^{-12}$ in Figure 16(a), which implies strongly localized strain fields. This strained region becomes shallower with an increase of the bulk regularization parameter $\xi = 10^{-2}$ (Figure 16)(b)).

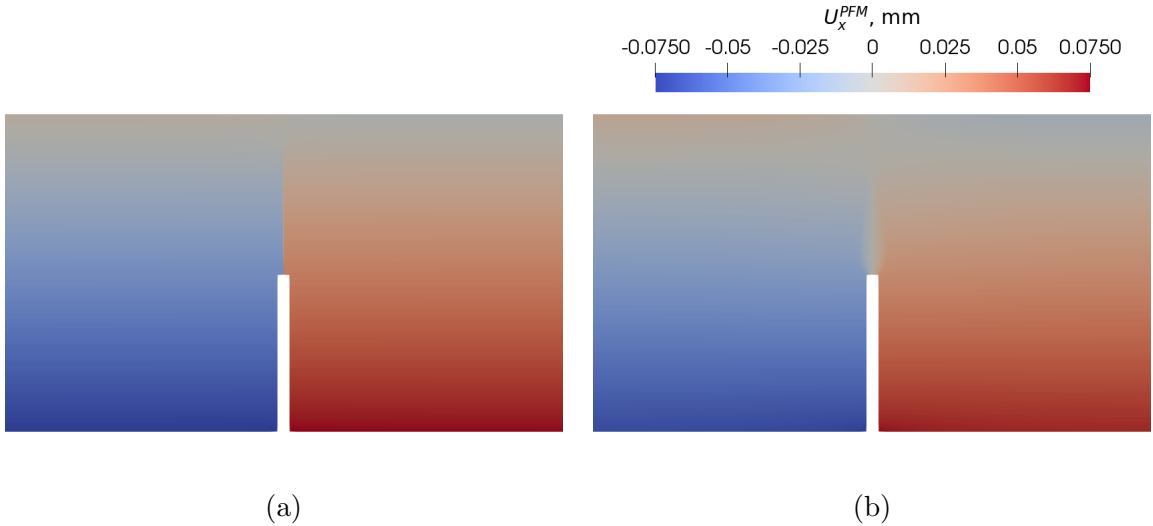


Figure 16: Influence of the bulk regularization parameter ξ on the phase-field displacement field in the x -direction when $t = 50$ s with $\ell_\varphi = 4.4$ mm on a mesh with $N_{ref} = 5$. Only the zone close to the notch (i.e., from 310 mm to 450 mm in the x -direction) is shown for the sake of legibility. (a) $\xi = 10^{-12}$ and (b) $\xi = 10^{-2}$

It may be anticipated that with a smoother displacement field, the identification results differ. Figure 17 shows the effect of ξ on the equivalent fracture mechanics parameters. The low RMS

displacement residuals, when $\xi \leq 10^{-5}$ (Figure 17(a)) show that the regularization parameter does not affect the levels of equivalent fracture parameters. Besides, the value of ξ does not influence the crack length and energy release rate histories (Figures 17(b,c)) when $\xi \leq 10^{-5}$. This observation also applies to the FPZ size (Figures 17(d)).

Large values of ξ reduce the crack length in the remainder of the test. Because the crack length is bigger for smaller values of ξ , the pacman reaches the top edge of the beam earlier than in the other cases, which means that the boundary effect (Section 5.3) occurs earlier. This effect is visible in the RMS displacement residuals displayed in Figure 17(a). The FPZ size (Figure 17(d)) is also affected; it decreases when ξ becomes small. It is concluded that the boundary effect from the phase-field model tends to reduce the size of the FPZ. One may also note that the size of the FPZ does not increase farther than the inner radius r_i of the pacman, which validates the choice of the pacman geometry.

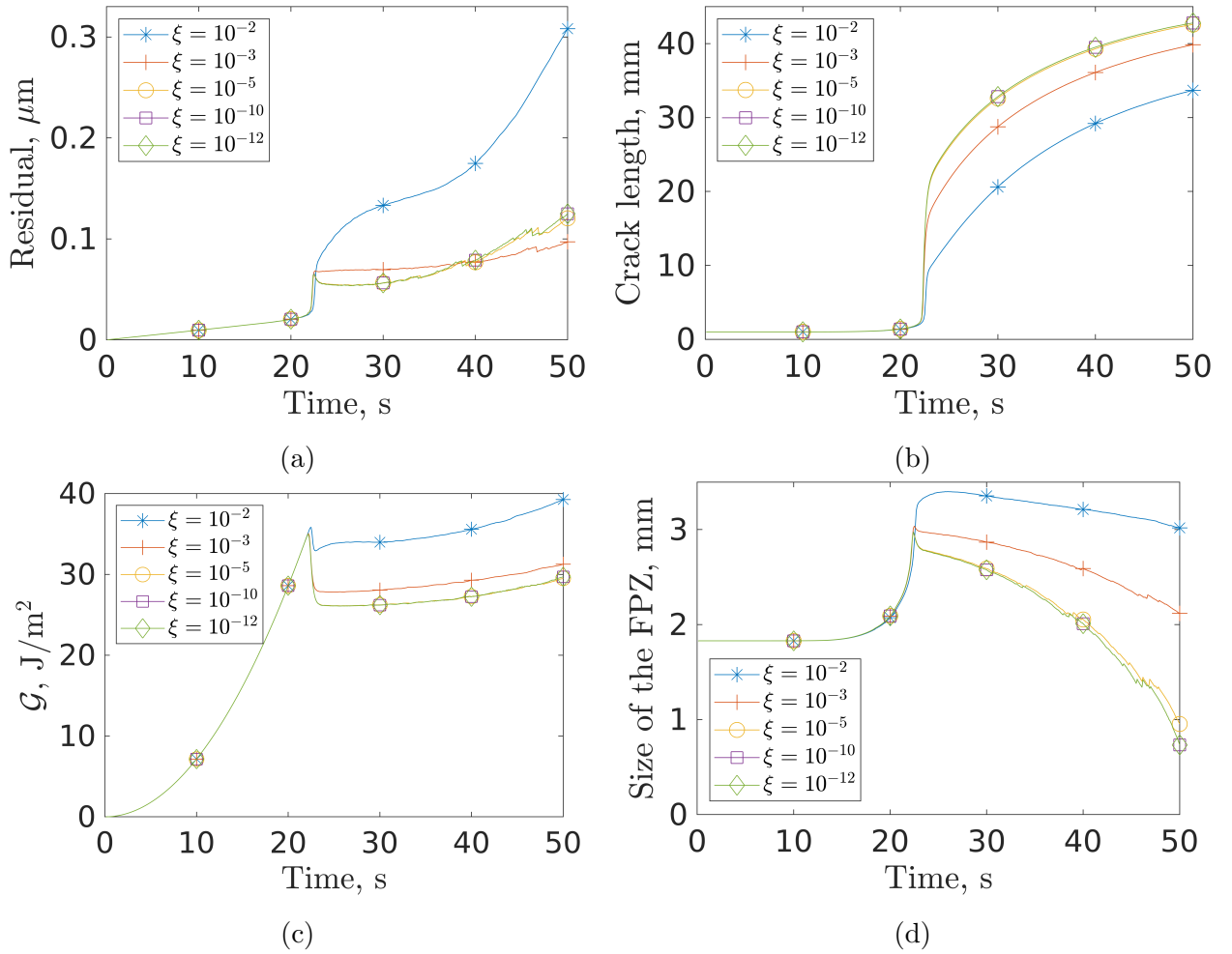


Figure 17: Influence of the regularization parameter ξ on the fracture parameters identified from phase-field calculations with $\ell_\varphi = 4.4$ mm and $N_{ref} = 5$ using Williams' series with Pacman 2 and mesh M3 with $N_0 = -3$ and $N_1 = 9$. (a) RMS displacement residuals, (b) crack length, (c) energy release rate, (d) size of the FPZ

The selection for the following analyses corresponds to FE simulations with $\delta t = 10$ ms and ξ equal to 10^{-10} . The phase-field simulation parameters are also gathered in Table 2. For the fracture mechanics analyses, Pacmen 2-6 (depending on ℓ_φ) are used with refinements according to mesh M3.

6 Extracting fracture mechanics parameters

The algorithm displayed in Figure 3 is first used to locate the crack tip. Williams' amplitudes γ_n (Equation (16)) are determined by minimizing the least square differences between Williams' solution and the phase-field displacement fields. The crack path is considered as a straight vertical line emanating from the middle of the notch root. Besides the crack length, this section further studies the equivalent energy release rate, stress intensity factors, and FPZ sizes. The results are reported for the five pacman meshes due to the different finite element meshes related to the internal length ℓ_φ (Table 2).

Figure 18(a) shows the RMS displacement residuals obtained from the least squares minimization with respect to the number of mesh refinements. The residuals corresponding to 2 or 3 refinements are significantly higher than those obtained with more refinements. Conversely, the residuals for 4 to 6 refinements are close and reach very low levels. The residuals increase suddenly at the beginning of crack propagation (ca. $t = 22 - 24$ s). Then, they decrease a bit before increasing again but more progressively. Before crack propagation, the smallest residuals are obtained for the smallest internal lengths. As the number of refinements increases, the residuals converge to very low levels. The highest residuals observed for the final time step remain very low (i.e., less than $0.15 \mu\text{m}$ for 4 to 6 mesh refinements) in comparison to the displacement amplitudes (i.e., $75 \mu\text{m}$ for the final propagation step). This result validates the proposed equivalence between phase-field simulations and the fracture mechanics kinematics away from the fracture process zone, especially for the smallest internal lengths.

Figure 18(b) displays the history of crack lengths $a(t)$ for each mesh. The number of mesh pre-refinements has a clear influence on the results. This observation was expected given the global response of the structure (Figure 8). The value of ℓ_φ has a small effect on the maximum crack length that tends to ≈ 4 cm when $\ell_\varphi \leq 8.8$ mm. The crack propagation onset is observed when the crack length increases quickly (i.e., ca. $t \geq 20$ s). The crack propagation onset time depends on the internal length ℓ_φ (between 20 s and 25 s); there is no clear trend between ℓ_φ and the onset of propagation. After a fast increase, the velocity of the crack gradually decreases. This observation means that propagation can be decomposed into fast followed by slow stages. Even though the NOD is controlled, it did not prevent fast crack growth from occurring at the onset of propagation.

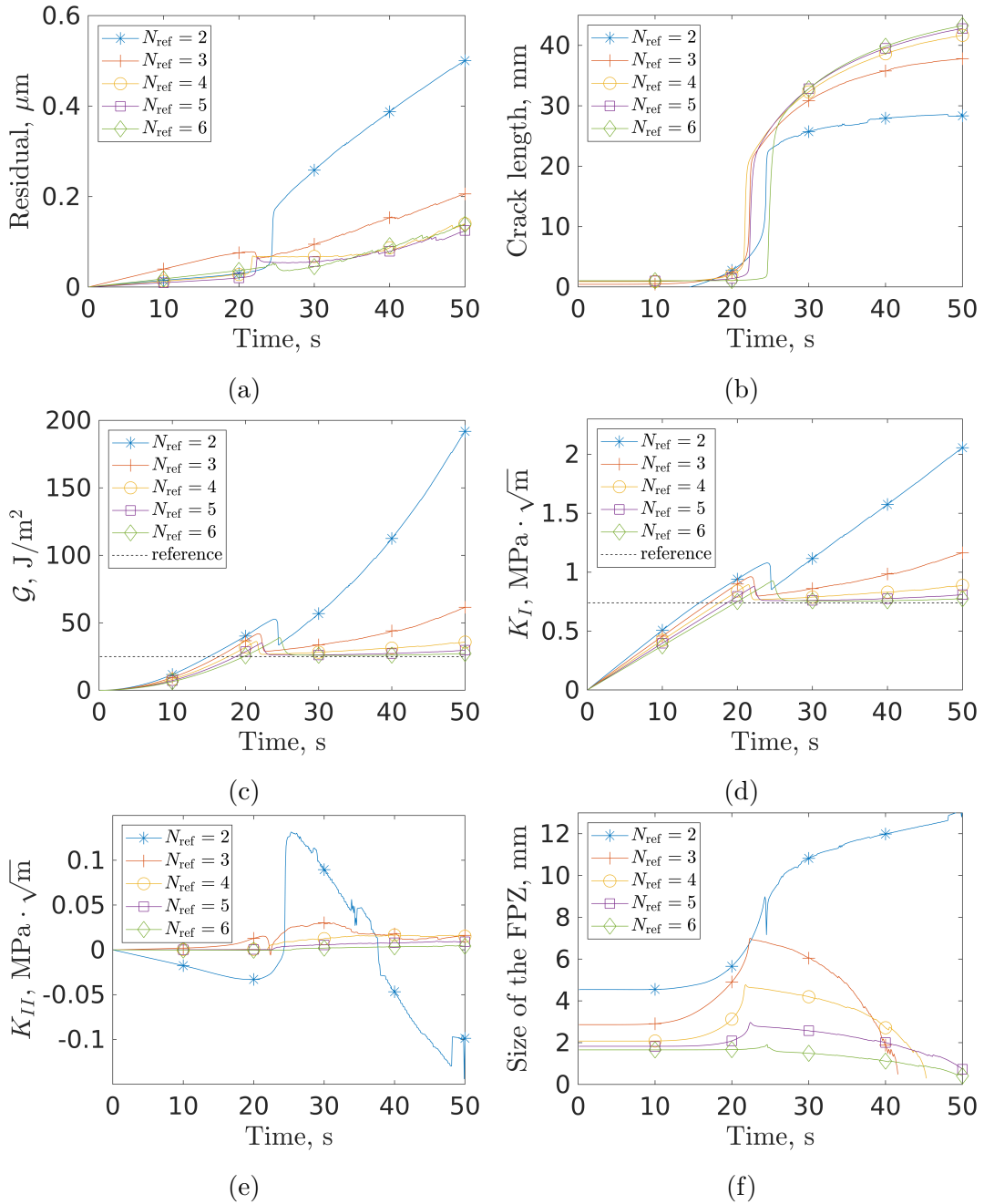


Figure 18: Identification results from phase-field simulations using meshes with 2, 3, 4, 5 or 6 pre-refinements (i.e., different internal lengths and corresponding pacman geometries, see Figure 9). (a) RMS displacement residuals, (b) crack length, (c) energy release rate, (d) mode I stress intensity factor, (e) mode II stress intensity, and (f) fracture process zone size as functions of time

In Figure 18(c), the histories of equivalent energy release rates are shown for each number of mesh refinements (and thus different internal lengths). The evolution of \mathcal{G} vs. time converges as the number of refinements increases. A first increase of \mathcal{G} is observed until crack propagation occurs (when $t \approx 20 - 25$ s) where \mathcal{G} falls off. This event coincides with the fast crack growth observed in Figure 18(b). Then, \mathcal{G} slightly increases again with time when the crack propagates on. The smaller the internal length, the steadier the energy release rate after the onset of propagation (and closer to the reference level, namely, $25 \text{ J}/\text{m}^2$). When the meshes are too coarse (i.e., using only 2 or 3

refinements) the energy release rate remains farther away from the lower bound observed for 5 and 6 refinements.

Figure 18(d,e) displays the SIF histories for modes I (K_I) and II (K_{II}). As expected, the levels of K_{II} are negligible compared to K_I for converged results. As for the previous variables, Figure 18(d) also illustrates the convergence of K_I with the number of mesh refinements for the phase-field model beyond the onset of propagation. The evolution of the stress intensity factor in mode I follows the same pattern as that of the equivalent energy release rate (Figure 18(c)). This result is expected with negligible mode II contributions (Figure 18(e)), as the SIF K_I then is proportional to the square root of the energy release rate \mathcal{G} . For K_{II} , the trend is also clear regarding convergence for different pre-refinements. For the finest refinements (i.e., lowest internal lengths), the offsets to the zero level (i.e., pure mode I) are lower.

The last parameter is the FPZ size indicator expressed by Equation (18)(Figure 18(f)). The FPZ size history is composed of two stages. First, before the crack propagates, there is a gradual increase related to the development of the damaged area around the notch root. In the second period when propagation occurs, different trends are observed depending on the mesh refinement. The FPZ size is stable, but slightly decreases over time when its extent becomes large and the pacmen reach the top edge of the beam. The FPZ size depends on the internal length ℓ_φ . The smaller the internal length, the smaller the FPZ size. For the coarser mesh, the FPZ size further increases after the onset of propagation. This trend is not found for the other four meshes.

The minimum energy release rate and SIF after propagation onset are reported in Figure 19. These levels depend on ℓ_φ and range from 34 J/m² and 0.85 MPa $\sqrt{\text{m}}$ for $\ell_\varphi = 36$ mm to 25.5 J/m² and 0.75 MPa $\sqrt{\text{m}}$ when $\ell_\varphi = 2.2$ mm, which is very close to the levels associated with a brittle material (i.e., 25 J/m² and 0.74 MPa $\sqrt{\text{m}}$). It is observed that the mode I SIF linearly depends on ℓ_φ (Figure 19(b)), and thus the energy release rate follows a quadratic evolution (Figure 19(a)). The coefficients of determination for the two regressions are $R^2 = 0.997$ (Figure 19(b)) and $R^2 = 0.998$ (Figure 19(a)), which indicate that both approximations are consistent with the corresponding data.

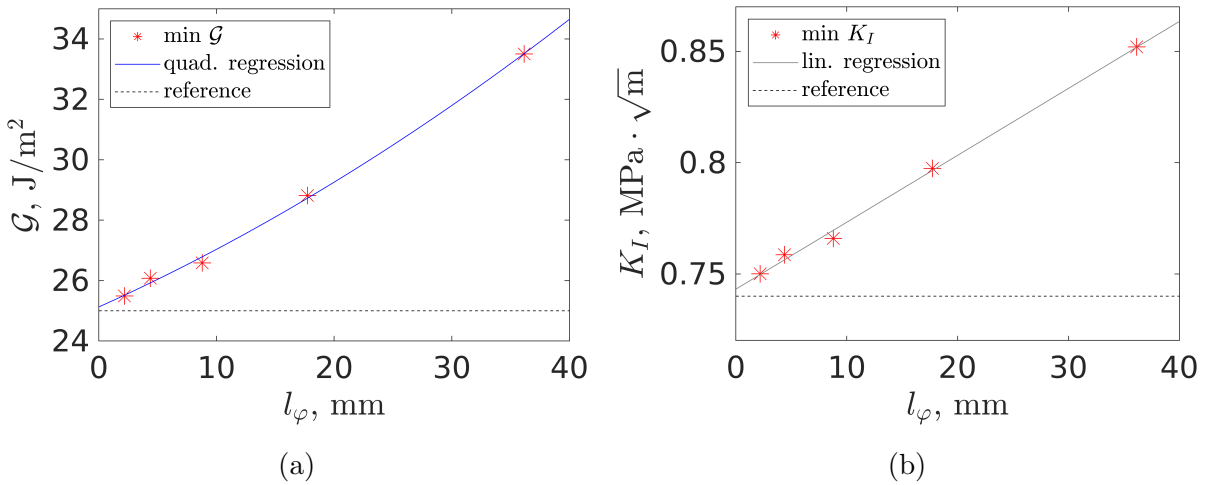


Figure 19: (a) Energy release rate and (b) mode I stress intensity factor as functions of the internal length of the phase-field model. The solid lines depict quadratic and linear regressions, respectively.

As shown in Figure 9(e), the inner radius of the pacmen was selected to exclude the FPZ. Figure 20(a) shows a comparison between their inner radius and the maximum FPZ size obtained using Williams' amplitudes (Equation (18)). The results validate the hypothesis that the pacman meshes lay outside of the FPZ (i.e., the FPZ size was always less than the inner radius). Hence, isotropic linear elasticity is applicable in the region covered by the pacman. Good consistency is reached between Williams' displacement fields and phase-field outputs in this region (i.e., very low residuals in the least squares minimization (Figure 18(a))). Figure 20(b) shows the change of the maximum FPZ size with the internal length ℓ_φ . The convergence with mesh refinements is excellent. The value of ℓ_φ affects, by construction, the extent of the region where $\varphi < 1$, and a linear trend is observed. For Figure 20(a), the determination coefficient is given by $R^2 = 0.989$ and the slope is equal to 0.66. For Figure 20(b), $R^2 = 0.996$ and the slope is 0.32. This last result shows that the estimator d_{FPZ} of the FPZ size extracted from the mode I supersingular field of order -3 (Equation (18)) is linearly related to the internal length ℓ_φ . These results further validate this estimator that was initially introduced for the analysis of an elastoplastic medium containing a crack [29].

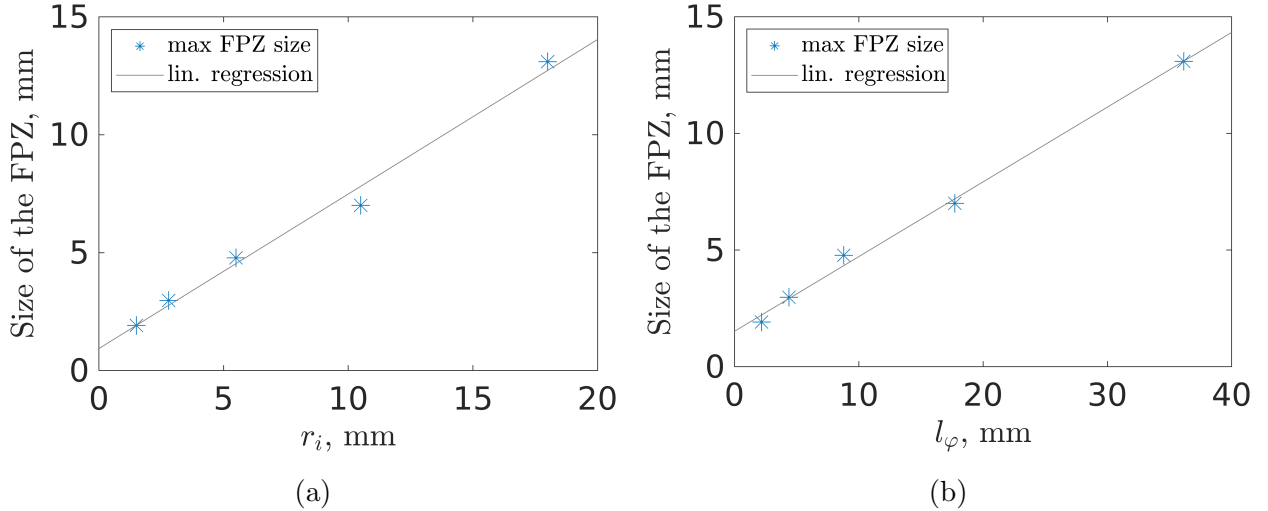


Figure 20: Maximum FPZ size identified over time from the phase-field results on meshes with 2, 3, 4, 5 or 6 pre-refinements for (a) different inner radii r_i of the pacmen and (b) different internal lengths ℓ_φ for the phase-field model

Last, the value of the phase-field variable at the crack tip is investigated using Williams' series results. The underlying question is whether a constant value of φ may be used as a simple criterion to locate the crack tip. The crack tip is not encoded in phase-field modeling and is estimated using approximations [17]. The analyses are based on meshes with five refinements (Figure 5). Williams' series give access to the crack tip positions and thus crack length (Figure 18(b)). The small displacement residuals (Figure 18(a)) give confidence in the previous estimates.

The phase-field variable is calculated at the estimated crack tip position (Figure 21(a)). The position of the crack tip is illustrated in Figure 21(b) and changes at every time step. The histories of the phase-field level at the crack tip are shown for all internal lengths ℓ_φ . Two parts in the curves are distinguished. The first part is before crack propagation. The choice of ℓ_φ has a limited influence

on the value of φ at the crack tip. After $t \approx 20$ s, the crack propagates. The value of φ at the crack tip slightly decreases with time for small internal lengths. The value of φ at the crack tip depends on the value of ℓ_φ . The lower ℓ_φ , the higher the phase-field value at the estimated crack tip position.

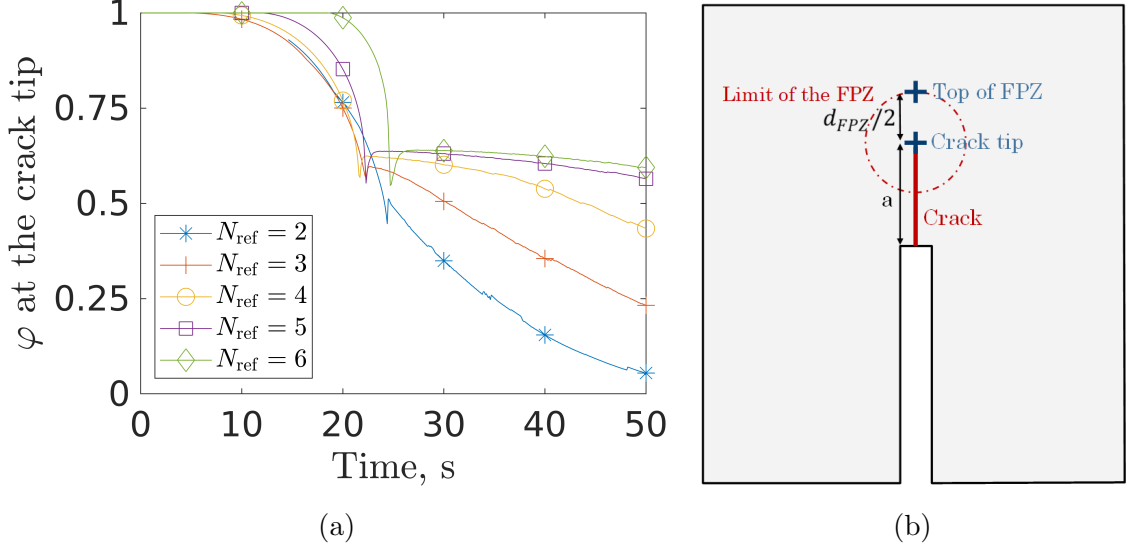


Figure 21: (a) Phase-field variable identified over time at the estimated crack tip position from phase-field results on meshes with different refinements. (b) Schematic view of the crack, the crack tip and the FPZ

In Figure 22(a), the changes with time of the phase-field value φ at the top point of the FPZ (vertical distance to the crack tip equal to $d_{FPZ}/2$, see Figure 21(b)) have similar overall changes for all internal lengths. The values depend on ℓ_φ . Figure 22(b) illustrates the effect of ℓ_φ on the mean value of φ at the identified crack tip at propagation onset (i.e., between $t = 25$ s and 30 s). The number of mesh refinements for the phase-field model has a strong influence on the results, and considering all meshes, the mean value of the phase-field converged for the last two refinements. The average phase-field value during propagation decreases according to the chosen value of the internal length. Therefore, the FPZ estimator cannot be obtained with any fixed value of φ .

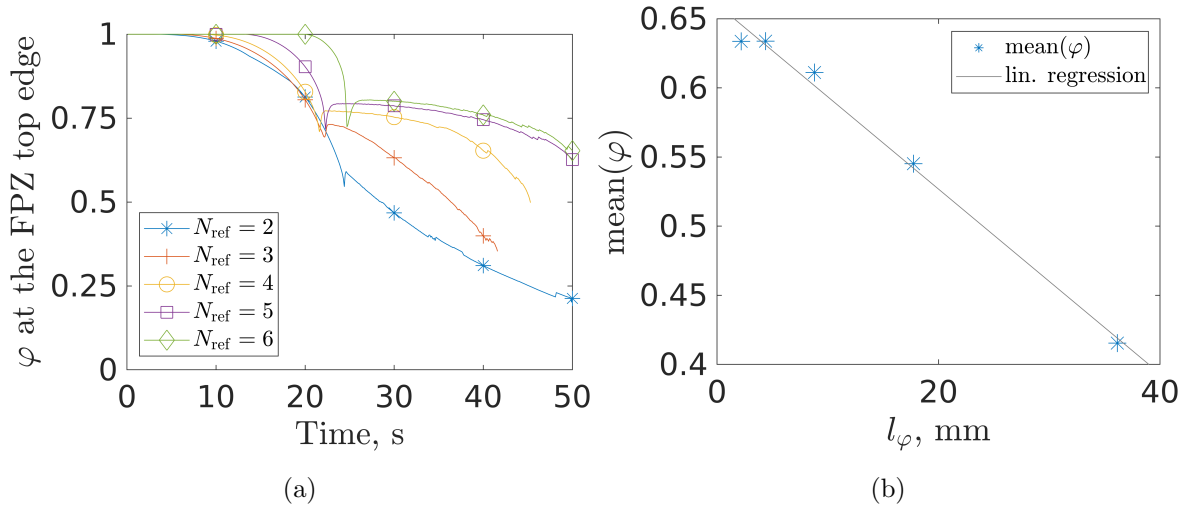


Figure 22: Phase-field values within the FPZ. (a) Phase-field value at the top of the FPZ (Figure 21(b)) as a function of time for different internal lengths. (b) Average phase-field value between $t = 25$ s and $t = 30$ s

7 Discussion

In this part, a discussion is provided about the main findings of the previous sections. Considering the notched beam, phase-field simulations were run with different meshes using uniform refinements with up to 1.5 million degrees of freedom. Even though the present implementations allow for local mesh refinements, it was decided to use uniform meshes to avoid the influence of different mesh levels and element sizes on the accuracy of the post-processing methodology. In line with other studies [13, 56, 25, 64, 20], the internal length l_φ was kept proportional to the minimum mesh size h_{min} by prescribing $l_\varphi = ch_{\text{min}}$ with $c = 16$. Variations were shown in other studies [26, 59, 27] (with different goals though).

Concerning the post-processing step with Williams' series, the unitary fields were constructed on a pacman geometry. The design of the pacman mesh is an important aspect of the analyses reported herein. The choice of inner radius was made *a priori* to ensure that the pacmen did not contain the FPZ. It was checked *a posteriori* that it was consistent with estimates of the FPZ size. The outer radius was selected to remain small enough to avoid edge effects as much as possible. Once the external radius was selected, the next step was to choose the truncation of Williams' series. The choice of the lower bound N_0 was dictated by the fact that $n = -3$ allows for an estimate of the FPZ size [29]. The upper bound N_1 was determined by performing a convergence study in terms of the crack length, energy release rate, and displacement residuals. Last, the level of discretization for the pacman mesh had a very limited effect on the residuals and all extracted fracture mechanics parameters.

One key novelty was the determination of crack tip positions. In the present analyses, it was based on the use of the first supersingular field as performed in digital image correlation analyses [24]. This approach differs from that proposed by Yoshioka et al. [64], which was based on surface energy equivalence. It was also shown herein that a simple criterion based on the phase-field variable could not be used to determine the crack tip position. It was not independent of time for a given internal

length and depended on the internal length.

Once the crack tip position was obtained, equivalent fracture mechanics parameters were determined for different internal lengths. Five mesh refinements proved sufficient in terms of RMS displacement residuals, which remained very low compared to the displacement amplitudes. This observation validated the use of Williams' series to analyze phase-field displacements in the vicinity (but outside) of the damaged zone. The levels of equivalent fracture energy and toughness were higher than the value used in the phase-field model, except for very small internal lengths. This trend was expected [13, 56, 64] as the energy is dissipated over a larger domain (i.e., the fracture process zone) than the equivalent crack surface. With the present framework, an estimate of the FPZ size was also possible. It was shown that it was linearly related to the internal length.

It was observed that the quality of the fracture mechanics parameter identification depended on the mesh size of the finite element mesh, and to a lesser degree on the pacman mesh. For the phase-field simulation meshes, one has to deal with discretization and regularization errors. On the one hand, the discretization errors increase as the element size increases. On the other hand, due to the h_{\min} dependence on ℓ_{φ} , the regularization error increases as well, which yields a smeared damage pattern. Depending on how coarse the mesh is chosen, the regularization error may lead to biased phase-field simulation results as a starting point for the post-processing analysis. To ensure an accurate parameter identification using the introduced method requires sufficiently fine finite element meshes. Such results could be obtained with a newly developed parallel matrix-free geometric multigrid preconditioner in order to cope with the computational cost. At the same time, the present findings indicate that care must be taken when too coarse meshes are utilized in phase-field fracture analyses as the accuracy of quantities of interest may be too low to be meaningful (Figure 18).

8 Conclusions

This work proposed a post-processing scheme for evaluating equivalent fracture mechanics parameters from phase-field simulations. Specifically, the phase-field transition zone (aka. fracture process zone) induces some challenges, in particular, the estimation of crack tip positions. To this end, Williams' series were employed to compute crack tip positions and other fracture mechanics quantities of interest such as energy release rate, stress intensity factors, and size of fracture process zones.

A quasi-static phase-field model was run for simulating crack initiation from a notch *and* propagation in quasi-brittle materials. A modern implementation with an efficient matrix-free geometric multigrid preconditioner of a combined active set Newton-GMRES method was used. This solver allowed multiple mesh levels to be investigated with (very) detailed computational convergence studies. The use of regularization led to the development of fracture process zones. Analyses were performed with different element sizes to evaluate the influence of the finite element discretization. Via least squares minimization, the simulated displacement fields were then projected onto Williams' basis written in a linear elastic fracture mechanics framework. Williams' series were assessed in pacman-like regions designed to exclude a first guess of the fracture process zone extent. The pacman was moved until being centered about the crack tip by canceling out the amplitude associated with the first

supersingular displacement field of Williams’ series. The residuals between the displacement fields of the phase-field simulations and Williams’ series were very small, which validated the proposed bridge. The size of the fracture process zone was also determined. When based on the third supersingular Williams’ field, it was shown that the estimator of the fracture process zone size was linearly correlated to the internal length of the phase-field model. Other parameters such as stress intensity factors and equivalent energy release rates were estimated as well. The influence of the pacman size and mesh density was studied and convergence was shown in terms of extracted parameters. They were complemented with temporal computational convergence studies in which a clear dependence on the choice of the time step sizes became visible.

The influence of the internal length was discussed as it directly determines the phase-field transition zone. The choice of the internal length directly affected the identified equivalent fracture mechanics parameters such as the onset of crack propagation, the energy release rate, the stress intensity factor and the size of the fracture process zone. As the internal length was decreased (and the element size accordingly), the previous quantities converged toward the brittle material limit. The internal length changed the level of the phase-field variable at the estimated crack tip positions, which shows that estimating the crack tip position from phase-field contours is not very reliable.

Acknowledgments

The financial support of the French-German University through the French-German doctoral college ‘Sophisticated Numerical and Testing Approaches’ (SNTA) is acknowledged under Grant Number CDFA-04-19. Discussions are acknowledged within the framework of the International Research Training Group on Computational Mechanics Techniques in High Dimensions GRK 2657 funded by the German Research Foundation (DFG) under Grant Number 433082294.

References

- [1] M. Ambati, T. Gerasimov, and L. De Lorenzis. A review on phase-field models of brittle fracture and a new fast hybrid formulation. *Computational Mechanics*, 55(2):383–405, 2015.
- [2] L. Ambrosio and V. Tortorelli. Approximation of functionals depending on jumps by elliptic functionals via γ -convergence. *Communications on Pure and Applied Mathematics*, 43:999–1036, 1990.
- [3] L. Ambrosio and V. Tortorelli. On the approximation of functionals depending on jumps by quadratic, elliptic functionals. *Bolletino dell Unione Matematica Italiana*, 6:105–123, 1992.
- [4] D. Arndt, W. Bangerth, D. Davydov, T. Heister, L. Heltai, M. Kronbichler, M. Maier, J.-P. Pelteret, B. Turcksin, and D. Wells. The deal.ii finite element library: Design, features, and insights. *Computers & Mathematics with Applications*, 2020.

- [5] D. Arndt, W. Bangerth, M. Feder, M. Fehling, R. Gassmüller, T. Heister, L. Heltai, M. Kronbichler, M. Maier, P. Munch, J.-P. Pelteret, S. Sticko, B. Turcksin, and D. Wells. The `deal.II` library, version 9.4. *Journal of Numerical Mathematics*, 30(3):231–246, 2022.
- [6] ASTM. E1820-11 standard test method for measurement of fracture toughness, 2011. ASTM, West Conshohocken, PA (USA).
- [7] R. Ballarini and G. Royer-Carfagni. Closed-Path J-Integral Analysis of Bridged and Phase-Field Cracks. *Journal of Applied Mechanics*, 83(6), 03 2016. 061008.
- [8] G. Barenblatt. The mathematical theory of equilibrium cracks in brittle fracture. *Advances in Applied Mechanics*, 7(C):55 – 129, 1962.
- [9] M. J. Borden, T. J. Hughes, C. M. Landis, and C. V. Verhoosel. A higher-order phase-field model for brittle fracture: Formulation and analysis within the isogeometric analysis framework. *Computer Methods in Applied Mechanics and Engineering*, 273(0):100 – 118, 2014.
- [10] B. Bourdin. Image segmentation with a finite element method. *Mathematical Modelling and Numerical Analysis*, 33(2):229–244, 1999.
- [11] B. Bourdin, G. Francfort, and J.-J. Marigo. Numerical experiments in revisited brittle fracture. *Journal of the Mechanics and Physics of Solids*, 48(4):797–826, 2000.
- [12] B. Bourdin and G. A. Francfort. Past and present of variational fracture. *SIAM News*, 52(9), 2019.
- [13] B. Bourdin, G. A. Francfort, and J.-J. Marigo. The variational approach to fracture. *Journal of Elasticity*, 91:5–148, 2008.
- [14] A. Braides. *Approximation of free-discontinuity problems*. Springer Berlin Heidelberg, 1998.
- [15] L. Cedolin, S. Dei Poli, and I. Iori. Experimental determination of the fracture process zone in concrete. *Cement and concrete research*, 13(4):557–567, 1983.
- [16] C. Chang and M. E. Mear. A boundary element method for two dimensional linear elastic fracture analysis. *International Journal of Fracture*, 74:219–251, 1995.
- [17] P. Diehl, R. Lipton, T. Wick, and M. Tyagi. A comparative review of peridynamics and phase-field models for engineering fracture mechanics. *Computational Mechanics*, 69(6):1259–1293, 2022.
- [18] P. H. Feenstra and R. De Borst. A composite plasticity model for concrete. *International journal of solids and structures*, 33(5):707–730, 1996.
- [19] G. Francfort and J.-J. Marigo. Revisiting brittle fracture as an energy minimization problem. *Journal of the Mechanics and Physics of Solids*, 46(8):1319–1342, 1998.
- [20] F. Freddi and L. Mingazzi. Mesh refinement procedures for the phase field approach to brittle fracture. *Computer Methods in Applied Mechanics and Engineering*, 388:114214, 2022.

- [21] T.-P. Fries and T. Belytschko. The extended/generalized finite element method: An overview of the method and its applications. *International Journal for Numerical Methods in Engineering*, 84:253–304, 2010.
- [22] B. Giovanardi, A. Scotti, and L. Formaggia. A hybrid xfem–phase field (xfield) method for crack propagation in brittle elastic materials. *Computer Methods in Applied Mechanics and Engineering*, 320:396–420, 2017.
- [23] A. A. Griffith. VI. The phenomena of rupture and flow in solids. *Philosophical transactions of the royal society of london. Series A, containing papers of a mathematical or physical character*, 221(582-593):163–198, 1921.
- [24] R. Hamam, F. Hild, and S. Roux. Stress intensity factor gauging by digital image correlation: Application in cyclic fatigue. *Strain*, 43:181–192, 2007.
- [25] A. C. Hansen-Dörr, R. de Borst, P. Hennig, and M. Kästner. Phase-field modelling of interface failure in brittle materials. *Computer Methods in Applied Mechanics and Engineering*, 346:25–42, 2019.
- [26] T. Heister, M. F. Wheeler, and T. Wick. A primal-dual active set method and predictor-corrector mesh adaptivity for computing fracture propagation using a phase-field approach. *Computer Methods in Applied Mechanics and Engineering*, 290:466–495, 2015.
- [27] T. Heister and T. Wick. Parallel solution, adaptivity, computational convergence, and open-source code of 2d and 3d pressurized phase-field fracture problems. *PAMM*, 18(1):e201800353, 2018.
- [28] T. Heister and T. Wick. pfm-cracks: A parallel-adaptive framework for phase-field fracture propagation. *Software Impacts*, 6:100045, 2020.
- [29] C. Henninger, S. Roux, and F. Hild. Enriched kinematic fields of cracked structures. *International Journal of Solids and Structures*, 47(24):3305–3316, 2010.
- [30] A. Hillerborg, M. Modéer, and P.-E. Petersson. Analysis of crack formation and crack growth in concrete by means of fracture mechanics and finite elements. *Cement and concrete research*, 6(6):773–781, 1976.
- [31] A. Hrennikoff. Solution of problems of elasticity by the framework method. *Journal of Applied Mechanics, Transactions ASME*, 8(4):A169 – A175, 1941.
- [32] X. Z. Hu and F. Wittmann. Fracture energy and fracture process zone. *Materials and Structures*, 25:319–326, 1992.
- [33] M. Jirásek. Nonlocal models for damage and fracture: Comparison of approaches. *International Journal of Solids and Structures*, 35(31):4133–4145, 1998.

- [34] D. Jodlbauer, U. Langer, and T. Wick. Matrix-free multigrid solvers for phase-field fracture problems. *Computer Methods in Applied Mechanics and Engineering*, 372:113431, 2020.
- [35] L. Kolditz and K. Mang. On the relation of gamma-convergence parameters for pressure-driven quasi-static phase-field fracture. *Examples and Counterexamples*, 2:100047, 2022.
- [36] L. Kolditz, K. Mang, and T. Wick. A modified combined active-set Newton method for solving phase-field fracture into the monolithic limit. *Computer Methods in Applied Mechanics and Engineering*, 414:116170, 2023.
- [37] L. M. Kolditz and T. Wick. Matrix-free geometric multigrid preconditioning of combined newton-gmres for solving phase-field fracture with local mesh refinement, 2024.
- [38] V. Kosin, A. Fau, C. Jailin, F. Hild, and T. Wick. Parameter identification of a phase-field fracture model using integrated digital image correlation. *Computer Methods in Applied Mechanics and Engineering*, 420:116689, 2024.
- [39] C. Kuhn and R. Müller. A continuum phase field model for fracture. *Engineering fracture mechanics*, 77(18):3625 – 3634, 2010.
- [40] A. Kumar, B. Bourdin, G. A. Francfort, and O. Lopez-Pamies. Revisiting nucleation in the phase-field approach to brittle fracture. *Journal of the Mechanics and Physics of Solids*, 142:104027, 2020.
- [41] H. Leclerc, J. Neggers, F. Mathieu, F. Hild, and S. Roux. *Correli 3.0*. IDDN.FR.001.520008.000.S.P.2015.000.31500, Agence pour la Protection des Programmes, Paris (France), 2015.
- [42] J. Lemaitre and J. Dufailly. Damage measurements. *Engineering Fracture Mechanics*, 28(5-6):643–661, 1987.
- [43] H.-G. Maschke and M. Kuna. A review of boundary and finite element methods in fracture mechanics. *Theoretical and Applied Fracture Mechanics*, 4(3):181 – 189, 1985.
- [44] J. Mazars. A description of micro-and macroscale damage of concrete structures. *Engineering Fracture Mechanics*, 25(5-6):729–737, 1986.
- [45] S. McNeill, W. Peters, and M. Sutton. Estimation of stress intensity factor by digital image correlation. *Engineering Fracture Mechanics*, 28(1):101–112, 1987.
- [46] C. Miehe, F. Welschinger, and M. Hofacker. Thermodynamically consistent phase-field models of fracture: variational principles and multi-field FE implementations. *International Journal for Numerical Methods in Engineering*, 83:1273–1311, 2010.
- [47] N. Moes, J. Dolbow, and T. Belytschko. A finite element method for crack growth without remeshing. *International Journal for Numerical Methods in Engineering*, 46:131–150, 1999.

- [48] G. Molnár, A. Doitrand, R. Estevez, and A. Gravouil. Toughness or strength? Regularization in phase-field fracture explained by the coupled criterion. *Theoretical and Applied Fracture Mechanics*, 109:102736, 2020.
- [49] N. I. Muskhelishvili et al. *Some basic problems of the mathematical theory of elasticity*, volume 15. Noordhoff Groningen, 1953.
- [50] T. Nguyen, J. Yvonnet, Q.-Z. Zhu, M. Bornert, and C. Chateau. A phase-field method for computational modeling of interfacial damage interacting with crack propagation in realistic microstructures obtained by microtomography. *Computer Methods in Applied Mechanics and Engineering*, 312:567 – 595, 2016.
- [51] J. R. Rice. A Path Independent Integral and the Approximate Analysis of Strain Concentration by Notches and Cracks. *Journal of Applied Mechanics*, 35(2):379–386, 06 1968.
- [52] S.-N. Roth, P. Léger, and A. Soulaïmani. A combined xfem–damage mechanics approach for concrete crack propagation. *Computer Methods in Applied Mechanics and Engineering*, 283:923–955, 2015.
- [53] S. Roux and F. Hild. Stress intensity factor measurements from digital image correlation: post-processing and integrated approaches. *International journal of fracture*, 140(1):141–157, 2006.
- [54] J. Scheel, D. Wallenta, and A. Ricoeur. A critical review on the complex potentials in linear elastic fracture mechanics. *Journal of Elasticity*, pages 1–18, 2022.
- [55] S. A. Silling. Reformulation of elasticity theory for discontinuities and long-range forces. *Journal of the Mechanics and Physics of Solids*, 48(1):175–209, 2000.
- [56] E. Tanné, T. Li, B. Bourdin, J.-J. Marigo, and C. Maurini. Crack nucleation in variational phase-field models of brittle fracture. *Journal of the Mechanics and Physics of Solids*, 110:80–99, 2018.
- [57] R. Vargas, J. Neggers, R. B. Canto, J. A. Rodrigues, and F. Hild. Analysis of wedge splitting test on refractory castable via integrated DIC. *Journal of the European Ceramic Society*, 36:4309 – 4317, 2016.
- [58] H. von Wahl and T. Wick. A high-accuracy framework for phase-field fracture interface reconstructions with application to stokes fluid-filled fracture surrounded by an elastic medium. *Computer Methods in Applied Mechanics and Engineering*, 415:116202, 2023.
- [59] T. Wick. Goal functional evaluations for phase-field fracture using PU-based DWR mesh adaptivity. *Computational Mechanics*, 57(6):1017–1035, 2016.
- [60] T. Wick. *Multiphysics Phase-Field Fracture: Modeling, Adaptive Discretizations, and Solvers*. De Gruyter, Berlin, Boston, 2020.

- [61] M. L. Williams. On the stress distribution at the base of a stationary crack. *Journal of Applied Mechanics*, pages 109–114, 1957.
- [62] F. H. Wittmann and X. Hu. Fracture process zone in cementitious materials. *International Journal of Fracture*, 51:3–18, 1991.
- [63] J.-Y. Wu, V. P. Nguyen, C. T. Nguyen, D. Sutula, S. Sinaie, and S. P. Bordas. Phase-field modeling of fracture. *Advances in Applied Mechanics*, 53:1–183, 2020.
- [64] K. Yoshioka, D. Naumov, and O. Kolditz. On crack opening computation in variational phase-field models for fracture. *Computer Methods in Applied Mechanics and Engineering*, 369:113210, 2020.